



HAL
open science

Physical and microstructural impacts on the hydro-mechanical behaviour of Ypresian clays

X.P. Nguyen, Yu-Jun Cui, Anh Minh A.M. Tang, X.L. Li, L. Wouters

► **To cite this version:**

X.P. Nguyen, Yu-Jun Cui, Anh Minh A.M. Tang, X.L. Li, L. Wouters. Physical and microstructural impacts on the hydro-mechanical behaviour of Ypresian clays. *Applied Clay Science*, 2014, 102, pp.172-185. <10.1016/j.clay.2014.09.038>. <hal-01119445>

HAL Id: hal-01119445

<https://enpc.hal.science/hal-01119445v1>

Submitted on 23 Feb 2015

HAL is a multi-disciplinary open access archive for the deposit and dissemination of scientific research documents, whether they are published or not. The documents may come from teaching and research institutions in France or abroad, or from public or private research centers.

L'archive ouverte pluridisciplinaire **HAL**, est destinée au dépôt et à la diffusion de documents scientifiques de niveau recherche, publiés ou non, émanant des établissements d'enseignement et de recherche français ou étrangers, des laboratoires publics ou privés.



HAL Authorization

29 **Abstract:** An experimental characterisation on Ypresian clays that are considered as one of the
30 potential geological host formations for the radioactive waste disposal in Belgium has been
31 carried out. Physical, microstructural, hydraulic and mechanical properties were investigated on
32 the samples taken from a cored borehole at Kallo in the Northern Belgium at 290 - 400 m depth.
33 Identification tests, scanning electron microscopy (SEM), mercury intrusion porosimetry (MIP)
34 and oedometer tests were performed. The results obtained showed that Ypresian clays are highly
35 plastic and their physical and mineralogical properties present significant variations over depth.
36 Compared to Boom Clay, the other potential host formation for the radioactive waste disposal in
37 Belgium, Ypresian clays show (i) clearly higher liquid limit and specific surface, especially for
38 its basal part ; (ii) lower density despite its deeper location; and (iii) lower degree of saturation of
39 samples. These features were related to a bi-modal pore-size distribution which is quite particular
40 for a sediment at such depth. Furthermore, it has been observed that the compressibility and
41 swelling capacity of Ypresian clays increase with depth while the permeability decreases despite
42 the increase in void ratio. The normalized compression curves confirm the soil compressibility
43 variations over depth and the slightly over-consolidated state of Ypresian clays.

44 Keywords: Ypresian clays; physical properties; microstructure; hydro-mechanical behaviour.

45

46

47

48

49 **1. Introduction**

50 Ypresian clays, situated between 290 - 400 m depth at Kallo (Northern Belgium), are considered
51 as a potential host formation in the Belgian high-level and/or long-lived (HL/LL) radioactive
52 waste disposal program. As opposed to the situation of Boom Clay, another potential host
53 formation which has been extensively investigated since the seventies in the laboratory and also
54 *in situ* in the “High Activity Disposal Experimental Site” Underground Research Laboratory
55 (HADES URL), the characterisation of Ypresian clays has been quite limited: before 1997,
56 geotechnical data on Ypresian clays were scarce and scattered as only few boreholes reaching the
57 bottom of the formation had been drilled by the Geological Survey of Belgium and other bodies
58 for different purposes. The first investigation campaign on Ypresian clays in the framework of
59 the research & development programme of radioactive waste disposal was started in 1997 - 1998
60 with several cored boreholes at the Doel site, situated in the North of the Antwerp city. This
61 campaign focused on the mineralogy, geochemistry, hydrology and physical properties (Van
62 Marcke and Laenen, 2005). Several boreholes were drilled at Kallo in 2008 - 2009 (Cammaer et
63 al., 2009), about 10 km to the south of Doel, enabling the geomechanical characterisation of the
64 Ypresian clays.

65 In the present work, four cores of Ypresian clays taken at different depths from the ON-Kallo-1
66 borehole were characterised in terms of physical properties, microstructure features, hydraulic
67 and mechanical behaviours. Moreover, by analysing and integrating the data of Ypresian clays
68 gathered at Doel (see Van Marcke and Laenen, 2005), a complete description of the variations of
69 Ypresian clays’ physical and microstructural properties in the horizontal and vertical directions is
70 given, the impact of these variations on the hydro-mechanical behaviour was also analysed.

71 **2. Materials and experimental methods**

72 *2.1. Geological description*

73 The Ieper Group was deposited during the Ypresian period (55 - 49.6 million years ago) in the
74 northwestern half of Belgium. It outcrops in the southern part of the depositional area, gently
75 dips and thickens toward the Northeast (Figure 1). The group comprises three marine sediment
76 formations, Kortrijk, Tielt and Gent, and corresponds roughly to London clay in Southeast
77 London, the “argile des Flandres” and the “argile Plastique” in Northern France (Van Marcke
78 and Laenen, 2005).

79 The term “Ypresian clays” refers to the sediments deposited during Early and Middle Ypresian
80 times including the Kortrijk Formation (Members of Orchies, Roubaix and Aalbeke) and a part
81 of the overlying Tielt Formation (Kortemark Member; Figure 2). At the Kallo site, Ypresian
82 clays were found between 289 and 400 m below surface: the Kortemark Member between 289 -
83 303 m depth, Aalbeke Member 303 - 311 m, Roubaix Member 311 - 380 m and between 380 -
84 400 m depth the Orchies Member.

85 As Ypresian clays were deposited in a neritic environment in the southern border of the North
86 Sea, their properties are significantly influenced by the transgressive - regressive cycles during
87 their sedimentation: (i) the grading trend is fining-upward for transgression while coarsening-
88 upward for regression; and (ii) the clay-size mineralogy is composed of more kaolinite, illite and
89 chlorite (non-expansive clay minerals) for transgression due to a distant detrital population
90 source, but higher smectite for regression (Van Marcke and Laenen, 2005). The main
91 transgressive - regressive cycles corresponding to the Ypresian clays’ sedimentology at Kallo
92 were estimated as shown in Figure 2 (Cammaer et al., 2009; Van Marcke and Laenen, 2005).
93 Note that these main cycles can be further divided into several sub-cycles of higher resolution.

94 The burial history of Ypresian clays at Doel shows several deposition - erosion cycles, resulting
95 in a c.a. 50 m difference between the present depth and the maximum one in the history (Van
96 Marcke and Laenen, 2005). Considering the vicinity between the Doel site and the Kallo site, we
97 can consider that the two sites have a similar degree of over-consolidation.

98 It is noteworthy to distinguish the yield stress σ'_y from the pre-consolidation stress σ'_p (and thus,
99 correspondingly, the yield stress ratio $YSR = \sigma'_y/\sigma'_{v0}$ from the over-consolidation one $OCR =$
100 σ'_p/σ'_{v0}): (i) the latter results solely from mechanical unloadings, such as erosion or arising of
101 water table (geological over-consolidation). It is estimated based on the maximal burial depth in
102 the geological history; while (ii) the former involves, in addition, others geological phenomena,
103 for example creep, digenesis, weathering, cambering and valley bulging.... It can be determined
104 from oedometer test in the laboratory (Burland, 1990; Chandler, 2000). Naturally, $\sigma'_y \geq \sigma'_p$ and
105 $YSR \geq OCR$ (see Figure 16).

106 2.2. *Physical properties*

107 The four soil cores investigated in this study are from the borehole ON-Kallo-1 drilled by
108 ONDRAF/NIRAS in 2008 - 2009 (Cammaer et al., 2009), and they are indicated in Figure 2:
109 YK43 and YK64 are in the middle of the Roubaix Member, YK73 is in the lower part of the
110 Roubaix Member and YK95 is taken in the upper part of the Orchies Member. Note that the soil
111 cores were named by the initials of the formation and the site followed by its number in the
112 borehole. For instance, YK43 means core number 43 of Ypresian clays from the borehole at
113 Kallo. These cores were contained in PVC tubes of 96 mm in inner diameter and of 1 m in
114 length, and wrapped in vacuumed aluminium foil. The two ends of each PVC tube were not

115 sealed by wax; thus water loss would occur by evaporation before laboratory testing (2010 -
116 2011).

117 Figure 3 shows the particle-size distribution curves of the four adjacent cores (YK44, 63, 74 and
118 96) by laser technique (Vandenberghe, 2011). It appears that the clay-size ($< 2 \mu\text{m}$) fractions of
119 all cores are higher than 55 %. The Roubaix Member is known to be siltier (coarser) than the
120 Orchies (YK96) and Aalbeke Members, and this is clearly reflected in the granulometer curves.
121 The three Roubaix Member samples have a relatively similar granulometer distribution. It should
122 be noted that for a given soil, significant difference may exist between particle-size distribution
123 curves obtained by laser technique and by sieving and hydrometer, particularly for clayey soils
124 (Nguyen, 2013).

125 The mineralogical composition of the four previously mentioned cores by X-ray diffractometry
126 and cation exchange capacity (CEC) measurement (Co-hexamine technique) is presented in
127 Table 1 for the bulk mass and in

128 Table 2 for the clay-size fraction (Vandenberghe, 2011). It appears that the non-clay minerals
129 represent less than half in bulk mass, and the clay minerals are dominated by expansive ones
130 (smectite and interstratified illite - smectite) that represent more than 80 % in clay-size ($> 2 \mu\text{m}$)
131 fraction and about two thirds in bulk mass. Moreover, the total clay minerals and the expansive
132 ones are quite similar for these four cores.

133 The physical and index properties of YK 43, 64, 73 and 95 are presented in Table 3. The values
134 of Atterberg's limits of the Kallo samples (this study) together with those of Doel (Van Marcke
135 and Laenen, 2005) were used for establishing the classification of the Ypresian clays according
136 to ASTM (2006) (see Figure 4). It can be observed that the Ypresian clays are highly plastic at

137 both the Kallo site and the Doel site. In particular, a liquid limit higher than 130 is identified on
138 YK73 and YK95. A large variability over depth of soils is also observed for both sites: YK73
139 (lower part of the Roubaix Member) and YK95 (upper part of the Orchies Member) have clearly
140 higher values of liquid limit and plasticity index than YK43 and YK64 (middle part of the
141 Roubaix Member). This is in agreement with the blue methylene value (*VBS*) determined
142 according to AFNOR (1998) and the specific surface S_s deduced from *VBS* (Tran, 1980). A clear
143 distinction between these two groups of samples, (YK43, 64) and (YK73, 95), can also be
144 observed through other parameters presented in Table 3 such as unit mass ρ_0 , dry unit mass ρ_{d0} ,
145 void ratio e_0 , porosity n_0 and water content w_0 : the two upper cores (YK43, 64) show higher ρ_0
146 and ρ_{d0} (lower e_0 , n_0 and w_0) than the two lower ones (YK73, 95). The carbonate contents of
147 Ypresian clays are low, except for YK43 that has a particularly high value of 10.2 g/100g. The
148 degree of saturation S_{r0} is lower than 100% for all samples, mainly owing to the water loss
149 during the sample conservation as stated above.

150 2.3. Microstructural properties

151 Figure 5 shows the Scanning Electron Microscope (SEM) photos of YK 43, 64, 73 and 95 on the
152 section perpendicular to the bedding plane. A dominance of silt grains with size up to 10 μm are
153 identified for the two upper cores, especially for YK43. On the contrary, for the two lower cores,
154 a clay particle matrix is observed with dispersed silt grains. This is more or less consistent with
155 the grain-size distribution curves as shown in Figure 3: the fraction of particles larger than 10 μm
156 in (YK44, 63) is about 20 %, against only 15 % and 5 % in YK74 and YK96, respectively.
157 However, the important difference between YK74 and YK96 in grain-size distribution is not
158 observed in this SEM results.

159 Figure 6 shows the pore-size distribution (PSD) curves of YK43, 73 and 95 by mercury intrusion
160 porosimetry (MIP) in terms of intruded mercury void ratio e_m , defined as the ratio of mercury
161 intrusion volume V_m to soil solid volume V_s , versus the entrance diameter D as well as $\delta e_m / \delta \log D$
162 versus $\log D$. It should be noted that the MIP technique used can only cover a range of pore sizes
163 from $D = 300$ to $0.005 \mu\text{m}$, corresponding to a range of injection pressure from 0.1 to 200 MPa,
164 and that the MIP tests on YK95 and YK43 were prematurely stopped due to a technical problem.
165 It is observed that YK73 (lower part of the Roubaix Member) and perhaps YK95 (upper part of
166 the Orchies Member) present bi-modal porosity with the density of the micro-pore family ($D =$
167 $0.06 \mu\text{m}$ for YK73) clearly higher than that of the second family ($D = 0.25 \mu\text{m}$). The pore-size
168 family around $D = 100 \mu\text{m}$ can be explained by the technical perturbation during the preparation
169 of samples. By contrast, YK43 (middle part of the Roubaix Member) shows a mono-modal
170 porosity with a sole dominant pore family of $D = 0.8 \mu\text{m}$. A macro-pore family at $D = 5 \mu\text{m}$ is
171 identified for YK43 but its density is negligible. This mono-modal porosity is typical for deep
172 sediments such as Boom Clay at Mol (Coll, 2005; Dehandschutter et al., 2004; Lima, 2011) and
173 at Essen (Nguyen, 2013).

174 *2.4. Experimental methods for investigating the hydro-mechanical behaviour*

175 Both high- and low-pressure oedometers (HPO and LPO) were used. The LPO had only one lever
176 arm multiplying the load by 10 on the sample, allowing applying a vertical stress σ_v up to 3.2
177 MPa on a sample of 50 mm diameter. The HPO had a double lever arm with one lever arm
178 multiplying the load by 5 and the other by 10, allowing applying a vertical stress σ_v up to 64
179 MPa on a sample of 50 mm diameter.

180 The soil samples were hand-trimmed to reach the dimensions of 50 mm in diameter and 20 mm
181 in height. The initial states of the tested samples are shown in Table 4 with soil initial water
182 content w_0 , void ratio e_0 , porosity n_0 , degree of saturation S_{r0} and density ρ_0 as well as the void
183 ratio under the *in situ* vertical effective stress, $e_{\sigma'_{v0}}$. The HPO tests are numbered 1 while the
184 LPO tests are numbered 2. In order to account for the deformability of the loading system in the
185 HPO tests, calibration was carried out without sample in the oedometer cell following the same
186 loading path as shown in Figure 7.

187 Typical test procedures for HPO and LPO tests are presented in Figure 7 and Figure 8,
188 respectively. After installing the soil sample in the oedometer cell, step loading (A - B) up to the
189 *in situ* vertical effective stress σ'_{v0} , rounded for practical convenience to 3.2 MPa, was
190 undertaken without putting the sample in contact with water in order to avoid soil swelling which
191 would modify the soil microstructure (AFNOR, 1997; Delage et al., 2007; Deng et al., 2011a,
192 2011b, 2011c, 2012). Afterwards, the bottom porous stone and the drainage system were then
193 filled with synthetic Ypresian clays water (SYCW) consisting of 8.896 g NaCl and 0.896 g
194 Na_2SO_4 in 1 L solution (Van Marcke, 2009). For HPO tests, two stepwise unloading - reloading
195 loops between $\sigma_v = \sigma'_{v0}$ (C) - 0.2 (D) - 16 (E) - 0.2 (F) - 32 (G) MPa and a final unloading from
196 $\sigma_v = 32$ MPa (G) to 0.2 MPa (H) were then undertaken (Figure 7). For LPO tests, unloading from
197 σ'_{v0} to 0.05 MPa (C-D), reloading from 0.05 MPa to 3.2 MPa (D-E) and unloading again to 0.05
198 MPa (E-F) were conducted (Figure 8). The French standard (AFNOR, 1997) was applied for the
199 volume change criterion: the volume change was considered as steady when the vertical strain
200 rate was lower than $5 \times 10^{-4}/8$ h.

201 3. Experimental results

202 3.1. Compressibility and swelling capacity

203 Low- and high-pressure oedometer compression curves of YK43, 64, 73 and 95 are presented in
204 Figure 9, 10, 11 and 12, respectively. The values of degree of saturation S_r during the initial
205 loading (AB), before soaking (putting in contact with SYCW), were determined by assuming a
206 constant water content $w = w_0$ and indicated on the curves. It appears that all soil samples
207 reached full saturation at the end of this process, under $\sigma_v = \sigma'_{v0} = 3.2$ MPa, except the YK64O1
208 sample with a final value of 98 % (Figure 10b). As all the curves are clearly non-linear, the
209 compression index C^*_c and swelling index C^*_s are adopted that correspond respectively to the
210 slopes of each (re)loading and unloading (Deng et al., 2011a). An increase of C^*_c when S_r
211 approaches 100 % is observed, especially for YK73 and 95. Le et al. (2011) conducted oedometer
212 tests on unsaturated Boom Clay samples with suction measurement and observed that this
213 increase in C^*_c corresponds to the suction becoming zero when pore water started to be squeezed
214 out.

215 Upon soaking, slight compressions are observed for all the tests. For YK64, 73 and 95, the void
216 ratios $e_{\sigma'_{v0}}$ under the *in situ* vertical effective stress $\sigma_v = \sigma'_{v0} = 3.2$ MPa (point C) in LPO and
217 HPO tests are almost the same (Table 4). On the contrary, for YK43, the value of $e_{\sigma'_{v0}}$ in LPO
218 test (0.64) is smaller than that in HPO test (0.70). Note that the YK43 sample in LPO test has a
219 smaller initial void ratio e_0 than that in HPO test (0.78 against 0.81), but this difference is smaller
220 than that under the *in situ* stress (0.03 against 0.06).

221 Upon the first unloading after soaking (C-D), two swelling fashions are identified: for YK43 and
222 64, the void ratio at the end of this unloading, under $\sigma_v = 0.21$ MPa in HPO test and 0.05 MPa in
223 LPO test (point D), is smaller than its initial value e_0 , while for YK73 and 95 the inverse is
10

224 observed, showing a higher swelling capacity than the two samples taken at upper depths. Note
225 that the densities of YK73 and 95 samples at the beginning of this unloading under $\sigma_v = 3.2$ MPa
226 (point C) are lower than those of YK43 and 64 samples (see Table 4).

227 For all the four samples at different depths, the compression curves upon this unloading (C-D)
228 are clearly non-linear as the swelling index C_s^* increases with the decrease of vertical stress σ_v .
229 A roughly bi-linear shape was adopted by Cui et al. (2013) with a small slope C_{sel} that
230 corresponds to a mechanical rebounding under high vertical stress and a larger slope C_{spl} that
231 corresponds to a physico-chemical swelling under lower vertical stress, the two parts being
232 separated by a swelling stress σ_{sl} (Figure 13).

233 During the first reloading (D-E), the non-linearity of the curve was considered by Cui et al.
234 (2013) as tri-linear: (i) when $\sigma_v < \sigma'_{v0} = 3.2$ MPa, the compression curve is bi-linear, formed by a
235 small compression (C_{cel}) under low vertical stresses and a significant compression (C_{cpl}) under
236 higher vertical stresses; (ii) when $\sigma_v > \sigma'_{v0} = 3.2$ MPa, the compression curve progressively joins
237 the virgin compression line defined by the common compression index C_c (see Figure 13).

238 For each unloading - reloading loop, two swelling stresses σ_s and four characteristic indices C_{se} ,
239 C_{sp} , C_{ce} , C_{cp} can be identified as illustrated in Figure 13. The yield stress σ'_y can be determined
240 according to the French standard (AFNOR, 1997) as the stress value corresponding to the
241 intersection between the virgin compression line and the line passing by point C (*in situ* state)
242 with the slope C_{sel} .

243 Figure 14 shows that the swelling stress σ_s for each unloading/reloading path, in HPO and LPO
244 tests, is well correlated with the corresponding initial void ratio e_i (the value before the unloading
245 or reloading).

246 In addition, a series of swelling tests with “zero swell” method (Sridharan et al., 1986) was
 247 carried out by UCLouvain (1998) on Ypresian clays of several depths at the Doel site. Since the
 248 positions of Ypresian formation at Kallo (Cammaer et al., 2009) and Doel (Van Marcke &
 249 Laenen, 2005) are different, “equivalent depth” was used to compare data of the two sites. Given
 250 D_K a depth in Ypresian formation at Kallo, belonging to a member delimited by depth H_{1K} on the
 251 top and depth H_{2K} at the bottom, and the corresponding limit depths of this member at Doel are
 252 H_{1D} and H_{2D} , the “equivalent depth” of D_K at Doel (D_{KD}) can be determined as follows:

$$253 \quad D_{KD} = \frac{D_K - H_{1K}}{H_{2K} - H_{1K}} \times (H_{2D} - H_{1D}) + H_{1D} \quad (1)$$

254 The swelling stress σ_s determined by “zero swell” method for the Ypresian clays at Doel at the
 255 equivalent depths, noted as YK43, 64, 73, 95-D, of the four studied cores are also presented in
 256 Figure 14 with the corresponding initial void ratio.

257 Linear relations between swelling stress σ_s and corresponding initial void ratio e_i are obtained in
 258 a semi-logarithmic plane for all the depths as observed by Cui et al. (2013). Moreover, good
 259 agreements between (i) Doel and Kallo sites (YK43 versus YK43-D and so on for YK64, 73 and
 260 95), and (ii) common swelling tests and LPO and HPO compression tests are observed for each
 261 depth. For a given initial void ratio e_i , YK73 and YK95 (lower part of the Roubaix Member and
 262 upper part of the Orchies Member) show a significantly higher swelling stress σ_s as compared to
 263 YK43 and 64 (the upper part of the Roubaix Member).

264 The variations of C_{se} and C_{ce} , C_{sp} and C_{cp} with the preconsolidation stress σ'_p for each
 265 unloading/reloading path are presented in Figure 15a and b, respectively. For the first unloading
 266 and reloading loop, as the soil is only slightly over-consolidated (see paragraph below), σ'_p was

267 rounded to $\sigma'_{v0} = 3.2$ MPa for simplicity. For the second and third unloading-reloading loops,
268 based on the stress path in HPO tests, σ'_p was taken equal to 16 and 32 MPa, respectively. It
269 appears that C_{se} and C_{ce} are independent of the pre-consolidation stress σ'_p (Figure 15a) while
270 C_{sp} and C_{cp} increase with the increase of σ'_p . It is observed that these four indices are similar for
271 YK43 and YK64. It is also the case for those of YK73 and YK95. C_{se} , C_{sp} and C_{cp} of YK43 and
272 YK64 are much smaller than those of YK73 and YK95, C_{ce} being the same for the four samples.
273 Furthermore, for YK43 and YK64, the differences between C_{se} and C_{ce} and between C_{sp} and C_{cp}
274 are not obvious. On the contrary, for YK73 and YK95, for a given σ'_p , $C_{se} > C_{ce}$ and $C_{sp} < C_{cp}$.

275 The variation over depth of compression index C_c and yield stress σ'_y of Ypresian clays at Kallo,
276 determined according to Figure 13, are presented in Figure 16. The yield stress ratio YSR and the
277 over-consolidation ratio OCR are also reported in this figure. It is observed that the
278 compressibility of Ypresian clays increases with depth within the Roubaix Member (Figure 16a).
279 The yield stress σ'_y profile with indication of YSR and OCR (Figure 16b) shows a good
280 correspondence between the geological study undertaken by Van Marcke & Laenen (2005) and
281 this mechanical characterisation: the Ypresian clays are slightly over-consolidated and the YSR
282 for each depth is a little higher than the corresponding OCR . It also suggests that diagenesis as
283 well as other geological events after deposition are of minor importance for the Ypresian clays.

284 In addition, the long-term behaviour of the Ypresian clays was also investigated in this study
285 through the secondary compression/swelling coefficient $C_{\alpha e} = -\Delta e / \Delta \log t$. Considering the
286 important role of the swelling stresses σ_s on the compression curve $e - \log \sigma_v$, a correlation
287 between $C_{\alpha e}$ with the ratio of vertical stress and swelling stress for the corresponding path σ_v / σ_s
288 (c.f. Figure 13) is analysed and presented in Figure 17 for both HPO and LPO tests. By

289 definition, $C_{\alpha e}$ is positive upon (re)loading and negative during unloading (see Deng et al.,
 290 2012). It appears that for each depth a unique relationship ($C_{\alpha e}$, σ_v/σ_s) can be adopted for
 291 different reloading (or unloading) paths of both HPO and LPO tests as sketch in the Figure 17.
 292 Similarity in ($C_{\alpha e}$, σ_v/σ_s) between YK73 and 95 and between YK43 and 64 can be observed so as
 293 only one trend line is adopted for the $C_{\alpha e}$ - σ_v/σ_s relation of each couple of cores in reloading (or
 294 unloading). It is clearly observed that $C_{\alpha e}$ increases with the increase of σ_v/σ_s . Furthermore, for a
 295 given σ_v/σ_s ratio, YK73 and YK95 show higher $C_{\alpha e}$, in absolute value, than YK43 and YK64.
 296 Taking into account the large lifespan of a radioactive waste disposal as well as significant
 297 delayed convergence monitored in URL galleries (Armand et al., 2013), these simple and
 298 efficient correlations would be of considerable interest for further investigation and modelling of
 299 the long-term behaviour of the geological barriers in the performance assessment framework.

300 3.2. Permeability

301 Based on the consolidation curves, the hydraulic conductivity k and permeability K were
 302 determined based on the Casagrande's method:

$$303 \quad k = \frac{C_v \rho_f g}{E_{oed}} \quad ; \quad K = \frac{k \mu_f}{\rho_f g} \quad (2)$$

304 where $C_v = 0.197H^2/t_{50}$ is the consolidation coefficient, H is the drainage length and t_{50} is the
 305 time corresponding to 50% consolidation degree; ρ_f is the unit mass of fluid; g is the acceleration
 306 due to gravity; E_{oed} is the oedometric modulus; and μ_f is the fluid dynamic viscosity.

307 The variations of hydraulic conductivity k and permeability K with void ratio are presented in
 308 Figure 18. It appears that for a given void ratio, the soil permeability decreases with depth within

309 the range considered. In particular, the permeability of YK73 and 95 at their highest void ratio (e
310 ≈ 1) is still lower than that of YK43 at its lowest void ratio ($e \approx 0.5$).

311 A series of permeability tests under isochore condition on Ypresian clays at Doel was conducted
312 by Aertsens et al. (2005). The results are reported in Figure 19 for different depths. The values
313 obtained in this study for the Kallo site are also presented in Figure 19 using the “equivalent
314 depths” D_{KD} (see Eq. (1)). It can be observed that the results of the two studies are comparable
315 for the lower and the middle parts of the Roubaix Member. However, for YK43 the hydraulic
316 conductivity found in this study is significantly higher than that from Aertsens et al. (2005). This
317 shows some limitation of the comparison based on the notion of equivalent depth.

318 3.3. Microstructure effect

319 According to Mitchell & Soga (2005), the soil microstructure is defined by particle arrangement
320 and inter-particle bonding. Burland (1990) proposed a normalization method for the compression
321 curve $e - \log \sigma'_v$ which allows eliminating the effect of mineralogy and thus evidencing the effect
322 of microstructure. As reconstituted clays have similar microstructure (Burland, 1990; Leroueil et
323 al., 1985; Hong et al., 2010, 2012), their compression curves depend only on their mineralogy
324 characterised by their plasticity. These curves can be normalized using the void index I_v defined
325 by:

$$326 \quad I_v = \frac{e - e_{100}^*}{e_{100}^* - e_{1000}^*} = \frac{e - e_{100}^*}{C_c^*} \quad (3)$$

327 where e_{100}^* and e_{1000}^* are the void ratios at $\sigma'_v = 100$ and 1000 kPa, respectively; $C_c^* = e_{100}^* - e_{1000}^*$ is
328 the compression index. These parameters can be empirically determined using the void ratio e_L at
329 liquid limit w_L (Burland, 1990; Chandler, 2000). The asterisk denotes properties of soils at

330 reconstituted state, considered as “intrinsic” and to be distinguished from the properties of soils
331 at natural state that are affected not only by the mineralogy but also by microstructure.

332 By definition, all normalized compression curves $I_v - \log \sigma'_v$ of reconstituted clays become a
333 unique line passing by two points (0; 100 kPa) and (-1; 1000 kPa), namely intrinsic compression
334 line - ICL (Figure 20). For natural clays, due to their microstructure developed along their
335 geological history, their normalized compression curves lie on the right of ICL. Their positions
336 depend on their sensitivity S_σ ranging generally from 1 for reconstituted soils to 10 (Cotecchia &
337 Chandler, 2000). An average line at $S_\sigma = 5$ was defined as sedimentation compression line (SCL)
338 by Burland (1990) and regarded as a typical relationship for marine sediments. Note that the
339 sedimentation compression curve (SCC) of a natural soil, which can only be determined from the
340 natural water content of undisturbed sample and thus cannot be reproduced in the laboratory, is
341 not necessarily the SCL, neither the normalized compression curve determined by oedometer test.

342 The normalized compression curves of Ypresian clays are presented in Figure 20. The star
343 symbols represent the *in situ* states. It appeared that differently from the *in situ* void ratio $e_{\sigma'_{v0}}$,
344 the *in situ* void index I_{v0} decreases with depth, and thus better represents the deposition process -
345 the deeper the soil, the lower its *in situ* void index. Similar remark was made by Skempton
346 (1970): the liquidity index $LI = (w - PL)/(LL - PL)$ is more representative of soil deposition
347 process than water content w .

348 A significant difference between the *in situ* states of YK43 and the three lower depths (YK64,
349 73, 95) can be observed: while (I_{v0}, σ'_{v0}) for YK43 is situated between the SCL and ICL with an
350 estimated SCC as indicated in Figure 20, the points (I_{v0}, σ'_{v0}) for (YK64, 73, 95) lie slightly
351 below the ICL. Their SCCs must then coincide with the ICL because all the SCC of natural soils

352 must be on the right of the ICL or at least coincide with it. Due to these positions, the normalized
353 compression curve of YK43 crosses its SCC before bending downward in parallel to the SCL
354 and ICL, while the curves of (YK64, 73, 95) approach the ICL and then followed it. According
355 to Baudet & Stallebrass (2004), the parallelism between the virgin compression curves and the
356 SCL and ICL suggests that Ypresian clays have stable structure, as opposed to the soils of meta-
357 stable structure which have virgin compression slopes steeper than those of SCL and ICL.

358 *3.4. Microstructure after test*

359 MIP test was conducted on the sample after test YK73O1, corresponding to the state at point H
360 in Figure 11b. The pore size distribution (PSD) curve for this sample is presented in Figure 21.
361 The PSD curve of intact YK73 sample is also reported in this figure for reference. It appears that
362 after the HPO test, the nearly bi-modal PSD curve becomes almost a mono-modal one with a
363 dominant pore diameter around $D = 0.3 \mu\text{m}$. It is observed that the infra-pores (Romero, 1999)
364 with $D < 0.02 \mu\text{m}$ were not affected by the test, while meso-pores ($0.2 < D < 1 \mu\text{m}$) increased in
365 detriment of the micro-pores ($0.02 < D < 0.2 \mu\text{m}$) and the macro-pores ($D > 1 \mu\text{m}$). The pore-
366 size family around $D = 100 \mu\text{m}$ can also be explained by the technical perturbation during the
367 preparation of samples as for the intact sample.

368 The SEM photos on the sample after test YK43O2, corresponding to the state at point F in Figure
369 9a, are presented in Figure 22, together with those on the intact sample YK43. On the whole, the
370 bonded structure of the intact sample becomes less bounded after the mechanical loading in
371 saturated condition with well distinguished silt grains.

372 **4. Discussion**

373 *4.1. Physical and microstructural properties*

374 The particle-size distribution (Figure 3) and mineralogical analyses (Table 1 and 2) by
375 Vandenberghe (2011) showed that Ypresian clays are very fine-grained and highly plastic with
376 significant amount of expansive minerals. These features are represented by their particularly
377 high positions in the plasticity chart (Figure 4) and large values of initial void ratio e_0 , specific
378 surface S_s and VBS (Table 3) identified in this study and by Van Marcke & Laenen (2005).
379 However there is a discrepancy between the results obtained by Vandenberghe (2011) and the
380 results in the present study and Van Marcke & Laenen (2005) in terms of variability of these
381 properties. Indeed, according to Vandenberghe (2011), the differences in particle-size
382 distribution and especially in mineralogical composition for the Ypresian clays at Kallo are not
383 significant between the four depths. On the contrary, clear distinctions in terms of physical and
384 index properties between the two groups of depths – group 1: the middle of the Roubaix Member
385 (YK43 and YK64) and group 2: the lower part of the Roubaix Member (YK73) and the upper
386 part of the Orchies Member (YK95) (Figure 2) – were identified in the two latter studies: the
387 upper group (group 1) shows higher density but lower grain density ρ_s , consistence indices LL
388 and PI , specific surface S_s , blue methylene value VBS and water content w_0 than the lower group
389 (group 2). Furthermore, these variations of ρ_s , LL , PI , VBS , S_s and w_0 are better in line with the
390 geological history of Ypresian clays that is characterised by several transgressive - regressive
391 cycles (see section 2.1). Further studies on the particle size distribution and mineralogy of
392 Ypresian clays at Kallo are needed to clarify this point.

393 The SEM observations (Figure 5) also confirms the large difference between these two groups:
394 the microstructure of the lower group is dominated by clay particles with matrix type, while that

395 of the upper group shows the dominance of silt grains with aggregate type. A progressive
396 transition from the upper group to the lower one can be observed: the presence of clay fraction in
397 YK64 is more obvious than in YK43 but still less than in YK73. Note that the carbonate content
398 in YK43 (10 g/100g) is particularly higher than those in the three other depths. On the other
399 hand, the PSDs of YK73 and probably YK95 (the lower group), show bi-modality with a
400 dominant micro-pore family ($D = 0.06 \mu\text{m}$) at the intra-particle level and another dominant
401 meso-pore family ($D = 0.25 \mu\text{m}$) at the inter-particle level; the PSD of YK43 is mono-modal
402 with a sole dominant family of inter-particle pores having diameters as large as $D = 0.8 \mu\text{m}$.
403 These microstructural differences are in good agreement with the macroscopic observations: the
404 initial void ratio e_0 of the upper group are lower than those of the lower one that has higher
405 plasticity.

406 *4.2. Hydro-mechanical behaviour*

407 The results of odometer tests of Ypresian clays with unloading - reloading cycles are
408 characterised by clear hysteresis. According to Cui et al. (2013) and Nguyen (2013), these
409 hysteretic loops can be explained by the competition between physico-chemical and mechanical
410 effects that are separated by a threshold stress σ_s corresponding to the swelling stress. Note that
411 the term “mechanical” refers to the particle interactions through their direct contact, while the
412 term “physico-chemical” denotes the interactions between adsorbed water and clay particles.
413 Upon unloading, when the applied external stress is higher than the swelling stress ($\sigma_v > \sigma_s$), or
414 at the microscopic level the effect of the applied stress is stronger than that of the repulsive force
415 between clay particles/sheets, the particles contact mode would be rather of face-to-face. As a
416 result, the volumetric behaviour is rather controlled by the mechanical effect and small elastic
417 rebound occurs. On the contrary, when $\sigma_v < \sigma_s$, the physico-chemical effect prevails as particles

418 contact turns progressively into face-to-edge mode, giving rise to soil swelling with significant
419 volume change. Upon reloading, when the applied stress is lower than the swelling stress for this
420 path $\sigma_v < \sigma_s$, the face-to-edge particles contact microstructure is more or less preserved due to
421 the matrix suction caused by the physico-chemical effect, and small volume change occurs. By
422 contrast, when $\sigma_v > \sigma_s$, the mechanical effect prevails and larger volume change occurs by
423 collapse of large-pores, re-orienting particles contact to be more and more face-to-face mode.
424 Beyond the preconsolidation stress $\sigma_v > \sigma'_p$, the plastic volume change makes the particle re-
425 orientation more significant. Therefore, unloading from a higher preconsolidation stress σ'_p
426 induces higher swelling slope C_{sp} (see Figure 15b).

427 *4.2.1. Swelling capacity*

428 The higher positions of the $\log \sigma_s - e_i$ curves of YK73 and YK95 with respect to those of YK43
429 and YK64 in Figure 14 clearly distinguish the two groups in terms of swelling stress σ_s . In
430 addition, a unique correlation between e_i and σ_s may be expected with normalization by
431 mineralogy, like the normalisation by dry density of bentonite in the case of bentonite mixtures
432 (Agus, 2005; Dixon et al., 1996; Lee et al., 1999; Wang et al., 2012). Unfortunately, the
433 discrepancy in mineralogical composition (Vandenberghe, 2011) and physical properties
434 mentioned above does not allow this normalisation in the present study.

435 The increase of the swelling slope C_{sp} with the preconsolidation stress σ'_p
436 (see Figure 15) confirms the enhanced physico-chemical effect by mechanical loading (Le et al.,
437 2011): the larger the virgin compression, the more the orientation of clay particles (face-to-face
438 particles contact mode) and thus the stronger the physico-chemical interaction between clay

439 particles and adsorbed water. The following equation can be proposed to describe the increase of
 440 C_{sp} with σ'_p :

$$441 \quad C_{sp(\sigma'_p)} = \frac{C_c}{1 + \left(\frac{C_c}{C_{sp1}} - 1 \right) \times \exp \left(-\beta \ln \frac{\sigma'_p}{\sigma'_{p1}} \right)} \quad (4)$$

442 where β is a parameter which controls the increase rate of C_{sp} with σ'_p . For YK43, 64, 73 and 95,
 443 $\beta = 0.22, 0.42, 0.35$ and 0.35 , respectively; σ'_{p1} ($= 3.25$ MPa in this study) is a reference stress
 444 corresponding to $C_{sp} = C_{sp1}$. The Eq. (4)-based correlations are shown by dotted lines in Figure
 445 15b. It is observed that the values of C_{se} and C_{sp} as well as the slopes $\Delta C_{sp}/\Delta \sigma'_p$ of the two lower
 446 depths (YK73 and 95) are larger than those of the two upper depths (YK43 and 64), despite the
 447 lower densities of YK73 and 95. This again confirms the higher swelling capacity of YK73 and
 448 95.

449 The independence of C_{se} with respect to σ'_p confirms that the soil behaviour during unloading
 450 under $\sigma'_v > \sigma'_s$ is not significantly affected by the physico-chemical swelling, but characterised by
 451 the mechanical rebounding. This justifies the yield stress σ'_y determination method adopted in
 452 this study, avoiding inappropriate low values of σ'_y for deep sediments such as Boom Clay
 453 (Baldi et al., 1991; Deng et al., 2011b; Sultan et al., 2010) and London clay (Gasparre, 2005).
 454 Indeed, the values of σ'_y obtained in this study are in good agreement with the geological history
 455 characterised by the values of OCR . The slightly higher values of YSR with respect to OCR can
 456 reasonably be related to the creep effect developed during the geological history of several
 457 millions of years. The larger difference between YSR and OCR for YK73 (1.6/1.1) and 95
 458 (1.4/1.1) compared to those for YK43 (1.2/1.1) and 64 (1.5/1.2) (Figure 16b) indicates that creep

459 effect is more significant for the two lower cores than for the two upper ones. This is also
460 consistent with the higher swelling clay fraction of YK73 and YK95.

461 4.2.2. Compressibility

462 It is observed in Figure 15a that C_{ce} is independent of σ'_p and the mineralogy as the values are
463 quite similar for the four depths. This suggests that the microstructure characterised by the face-
464 to-edge particles contact mode that developed during the previous unloading was almost
465 preserved when $\sigma_v < \sigma_s$. This suggests also that the macroscopic volume change resulted mainly
466 from the compression of clay particles. Due to the competition between the increasing external
467 applied stress σ_v which tends to expel water from the clay particles and the physico-chemical
468 interaction between clay sheet and pore water which generates matrix suction retaining pore
469 water. The volume change in this stress range is thus negligible with $C_{ce} = 0.02$.

470 When the external applied stress is beyond the swelling stress $\sigma_v > \sigma_s$, the mechanical effect
471 prevails causing macro-pore collapse, giving rise to larger volume change with C_{cp} . Note that the
472 clay particle re-orientation in this stress range $\sigma_s < \sigma_v < \sigma'_p$ is less marked than in the virgin
473 compression domain where $\sigma_v > \sigma'_p$. Obviously, C_{cp} also increases with σ'_p and clay fraction as
474 observed in Figure 15. Moreover, the variation of C_{cp} must be limited by C_c on the upper side
475 and by C_{se} on the lower side because for a given σ'_p the higher the vertical stress σ_{vi} from which
476 the reloading is initiated, the lower the corresponding C_{cp} .

477 The increases of C_c (Figure 16a) and $C_{\alpha e}$ (Figure 17) with depth confirm the vertical variation of
478 the plasticity of Ypresian clays: the larger the consistence indices the larger the virgin and
479 secondary compression indices. This is in agreement with several correlations between
480 compression index and Atterberg limits in the literature for remoulded soils (Carrier, 1985;

481 Leroueil et al., 1984; Skempton, 1944; Terzaghi & Peck, 1967; Wroth & Wood, 1978) and also
482 natural clayey soils (Johnson & Moston, 1970).

483 4.2.3. Permeability

484 The permeability evolution of Ypresian clays at the Kallo site with depth is also in agreement
485 with the variations of soil mineralogy, grain-size distribution and microstructure: despite their
486 higher void ratios, YK73 and 95 show significantly lower permeability than YK43 and 64. This
487 can be explained by two reasons. From a microstructure point of view, the aggregate type fabric
488 and the dominance of macro-pores in YK43 and 64 form larger flow channel than the matrix
489 type fabric and the dominance of micro-pores in YK73 and 95 (Figure 6). From a mineralogical
490 point of view, water molecules in clay particles are associated with the exchangeable cations
491 adsorbed on the clay sheets forming the diffuse double layer. This affects the mobility of water
492 molecules and thus the permeability. Indeed, YK43 and 64 have similar void ratio (Table 4) and
493 microstructure type (Figure 5), but YK64 clearly shows lower permeability (Figure 18) because
494 of its higher plasticity index (Figure 4).

495 4.3. Microstructure effect on volumetric behaviour

496 The significantly higher positions of the *in situ* state (I_{v0} , σ'_{v0}) and the normalized compression
497 curve of YK43 with respect to those of YK64, 73 and 95 in the $I_v - \log \sigma_v$ plane can be related to
498 its lower clay fraction as observed on the SEM photos (Figure 5) and in the plasticity chart
499 (Figure 4), and its higher carbonate content (Table 3) which plays a decisive role in inter-particle
500 bonding. With the highest plasticity index and the lowest carbonate content, the normalized
501 compression curve of YK73 is logically the lowest one. The curve of YK95 is close to that of

502 YK73 albeit its higher carbonate content (3.8 against 0.9 g/100 g). This suggests that the effect
503 of carbonates in the microstructure can be compensated by that of expansive clay minerals.

504 According to Burland (1990), the stable microstructure of Ypresian clays (virgin compression
505 curves have the same slope as the SCL and ICL) indicates a quick deposition from a dense
506 suspension and/or under strong current. These depositional conditions would give rise to a more
507 oriented fabric thus more compact with a low void index I_v (not necessarily low void ratio e).

508 Particularly high expansive mineral content could also be the reason for the evolution of the PSD
509 curve, from nearly bi-modal for intact YK73 sample to nearly mono-modal for the sample after
510 the HPO test (Figure 21). Indeed, under compression at high pressures, clay particles were re-
511 oriented and fill the meso- and macro-pores. The porosity under high pressures became more and
512 more homogeneous with a sole dominant micro-pores. Upon unloading, due to the effect of
513 expansive minerals, the uniformity of the porosity was preserved as the dominant micro-pore
514 family swelled homogeneously to reach the size of meso-pores. On the contrary, due to the
515 limited amount of clay minerals, after the LPO test, the aggregate type microstructure of YK43
516 became even clearer as clay particles were only able to coat the silt grains, but not enough to
517 form a matrix. Therefore, the swelling upon unloading from $\sigma_v = \sigma'_{v0}$ consisted mainly in the
518 rebounding of the “frame structure” built by clay-coated silt grains, which is different from the
519 volume change mode of YK73. Thus, the void ratios at the end of the first unloading (point D) in
520 both LPO and HPO tests are much lower than the initial value $e_D < e_0$ for YK43 (Figure 9), but
521 higher than the initial value $e_D > e_0$ for YK73 (Figure 11).

522 **5. Conclusion**

523 The physical and geotechnical identifications, microstructure analysis and oedometer tests with
524 unloading-reloading loops have been performed on the samples of Ypresian clays cored at Kallo

525 (N-Belgium) in order to assess the Ypresian clays as a potential host formation for geological
526 disposal of radioactive wastes. Ypresian clays have been identified as fine-grained soil, highly
527 plastic, particularly porous with respect to their depths, and slightly carbonated except core
528 YK43.

529 Significant variability in terms of physical and geotechnical properties and microstructure have
530 been identified: i) the middle of the Roubaix Member (cores YK43 and YK64) presents lower
531 plasticity indices, void ratio e_0 , water content w_0 and higher density ρ_0 than the lower part of the
532 Roubaix Member (core YK73) and the upper part of the Orchies Member (core YK95); ii) the
533 microstructure of core YK43 (middle of the Roubaix Member) is characterized by the aggregate
534 type with dominance of the silty grains and a sole dominant meso-pore family at $D = 0.8 \mu\text{m}$.
535 The microstructure of core YK73 (lower part of the Roubaix Member) shows presence of a clay
536 matrix in which are dispersed silty grains, forming a bi-modal porosity with dominant micro-
537 pore ($D = 0.06 \mu\text{m}$) and meso-pore ($D = 0.25 \mu\text{m}$) families.

538 The oedometer compression curves of Ypresian clays are characterised by typical unloading -
539 reloading hysteretic loops, commonly observed for fine-grained soils in the literature. This
540 feature have been interpreted, according to Cui et al. (2013), by the competition between the
541 mechanical and physico-chemical effects which are separated by a swelling stress. This approach
542 allowed (i) properly determining the yield stress σ'_y of Ypresian clays at Kallo, which are in
543 good agreement with their geological history; (ii) better identifying the swelling capacity as well
544 as its dependence on their loading history. A semi-logarithmic linear relationship between the
545 swelling stress and initial void ratio, determined by common swelling tests and oedometer
546 compression tests were obtained. This confirmed the swelling stress concept proposed by Cui et

547 al. (2013) and showed the consistency between the different tests performed in this study as well
548 as the tests reported by Van Marcke & Laenen (2005).

549 The mechanical and hydraulic parameters deduced from oedometer tests showed significant
550 variation over depth: the compressibility and swelling capacity increases while the hydraulic
551 conductivity decreases over depth despite the increasing porosity. The normalised compression
552 curves in the $I_v - \log \sigma_v$ plane properly described the deposition process: the deeper the soil, the
553 lower its *in situ* void index I_{v0} . In addition, the Ypresian clays are characterised by stable
554 microstructure. The high carbonate content and aggregate type microstructure of YK43 were also
555 well identified by the distinct position of its $I_v - \log \sigma_v$ curve from those of the three other samples
556 in the ICL-SCL framework.

557

558 **6. References**

559 Aertsens, M., Dierckx, A., Put, M., Moors, H., Janssen, K., Van Ravestyn, L., De Cannière, P.,
560 2005. Determination of the hydraulic conductivity, η_R and the apparent diffusion
561 coefficient on Ieper Clay and Boom Clay cores from the Doel-1 and Doel-2b drillings.
562 Report No. SCK-CEN-R-3589 02/MAe/P-9, SCK-CEN.

563 AFNOR., 1997. Essai de compressibilité sur matériaux fins quasi saturés avec chargement par
564 paliers. XP P 94-090-1 (Vol. 1).

565 AFNOR., 1998. Mesure de la capacité d'adsorption de bleu de méthylène d'un sol ou d'un
566 matériau rocheux. Détermination de la valeur de bleu de méthylène d'un sol ou d'un
567 matériau rocheux par l'essai à la tache. NF P 94-068.

568 Agus, S., 2005. An experimental study on hydro-mechanical characteristics of compacted

569 bentonite-sand mixtures. Bauhaus-University Weimar.

570 Armand, G., Noiret, A., Zghondi, J., Seyedi, D.M., 2013. Short- and long-term behaviors of
571 drifts in the Callovo-Oxfordian claystone at the Meuse/Haute-Marne Underground
572 Research Laboratory. *Journal of Rock Mechanics and Geotechnical Engineering*, 5, 221-
573 230.

574 ASTM., 2006. Standard Practice for Classification of Soils for Engineering Purposes (Unified
575 Soil Classification System). ASTM D 2487 - 06.

576 Baldi, G., Hueckel, A., Peano, A., Pellegrini, R., 1991. *Developments in modelling of thermo-
577 hydro-geomechanical behaviour of Boom clay and clay-based buffer materials* (No. EUR
578 13964 EN). Commission of the European Communities.

579 Baudet, B., Stallebrass, S., 2004. A constitutive model for structured clays. *Géotechnique*, 54(4),
580 269-278.

581 Burland, J.B., 1990. On the compressibility and shear strength of natural clays. *Géotechnique*,
582 40(3), 329-378.

583 Cammaer, C., Cockaerts, G., Schiltz, M., 2009. *Drilling and geological report ON-KALLO-1,
584 ON-KALLO-2, ON-KALLO-3* (No. Samsuffit R2009-01). ONDRAF/NIRAS.

585 Carrier, W. D. (1985). Consolidation Parameters Derived From Index Tests. *Geotechnique*,
586 35(2), 211-213.

587 Chandler, R.J., 2000. Clay sediments in depositional basins: the geotechnical cycle (The 3rd
588 Glossop Lecture). *Quarterly Journal of Engineering Geology and Hydrogeology*, 33(1),
589 5-39.

- 590 Coll, C., 2005. Endommagement des roches argileuses et perméabilité induite au voisinage
591 d'ouvrage souterrains. Université Joseph Fourier-Grenoble 1, Grenoble.
- 592 Cotecchia, F., Chandler, R.J., 2000. A general framework for the mechanical behaviour of clays.
593 *Géotechnique*, 50(4), 431-447.
- 594 Cui, Y.J., Nguyen, X.P., Tang, A.M., Li, X.L., 2013. An insight into the unloading/reloading
595 loops on the compression curve of saturated clays. *Applied Clay Science*, 83-84, 343-348.
- 596 Dehandschutter, B., Vandycke, S., Sintubin, M., Vandenberghe, N., Gaviglio, P., Sizun, J.P.,
597 Wouters, L., 2004. Microfabric of fractured Boom Clay at depth: a case study of brittle-
598 ductile transitional clay behaviour. *Applied Clay Science*, 26, 389-401.
- 599 Delage, P., Le, T.T., Tang, A.M., Cui, Y.J., Li, X.L., 2007. Suction effects in deep Boom Clay
600 block samples. *Géotechnique*, 57, 239-244.
- 601 Deng, Y.F., Cui, Y.J., Tang, A.M., Nguyen, X.P., Li, X.L., Van Geet, M., 2011a. Investigating
602 the pore-water chemistry effects on the volume change behaviour of Boom clay. *Physics
603 and Chemistry of the Earth*, 36, 1905- 1912.
- 604 Deng, Y.F., Tang, A.M., Cui, Y.J., Nguyen, X.P., Li, X.L., Wouters, L., 2011b. Laboratory
605 hydro-mechanical characterisation of Boom Clay at Essen and Mol. *Physics and
606 Chemistry of the Earth*, 36, 1878- 1890.
- 607 Deng, Y.F., Tang, A.M., Cui, Y.J., Li, X.L., 2011c. Study on the hydraulic conductivity of Boom
608 clay. *Canadian Geotechnical Journal*, 48, 1491-1470.
- 609 Deng, Y.F., Cui, Y.J., Tang, A.M., Li, X.L., Sillen, X., 2012. An experimental study on the
610 secondary deformation of Boom Clay. *Applied Clay Science*, 59-60, 19-25.

611 Dixon, D.A., Gray, M.N., Graham, J., 1996. Swelling and hydraulic properties of bentonites
612 from Japan, Canada and USA (pp. 5-8). Presented at the second International Congress
613 on Environmental Geotechnics, Osaka, Japan.

614 Gasparre, A., 2005. Advanced laboratory characterisation of London clay. Imperial College
615 London.

616 Hong Z.S., Yin J., Cui Y.J., 2010. Compression Behaviour of Reconstituted Soils at High Initial
617 Water Contents. *Géotechnique*, 60(9), 691-700.

618 Hong Z.S., Zeng L.L., Cui Y.J., Cai Y.Q., Cheng L., 2012. Compression Behaviour of Natural
619 and Reconstituted Clays. *Géotechnique*, 62(4), 291-301.

620 Johnson, A.I., Moston, R.P., 1970. Relationship of consolidation characteristics and Atterberg
621 limits for subsiding sediments in central California, USA. Presented at the International
622 Symposium on Land Subsidence.

623 Le, T.T., Cui, Y.J., Munoz, J.J., Delage, P., Tang, A.M., Li, X.L., 2011. Studying the stress-
624 suction coupling in soils using an oedometer equipped with a high capacity tensiometer.
625 *Front. Archit. Civ. Eng. China*, 5(2), 160-170.

626 Lee, J.O., Cho, W.J., Chun, K.S., 1999. Swelling Pressures of a Potential Buffer Material for
627 High-Level Waste Repository. *Journal of the Korean Nuclear Society*, 31, 139- 150.

628 Leroueil, S., Tavenas, F., Locat, J., 1984. Correlations between index tests and the properties of
629 remoulded clays. *Géotechnique*, 35(2), 223-229.

630 Leroueil, S., Tavenas, F., Locat, J., 1985. Discussion: Correlations between index tests and the
631 properties of remoulded clays. W. D. Carrier and J. F. Beckman. *Géotechnique*, 35(2),
632 223-226.

- 633 Lima, A., 2011. Thermo-Hydro-Mechanical behaviour of two deep Belgian clay formations:
634 Boom and Ypresian clays. Universitat Politècnica de Catalunya, Spain.
- 635 Mitchell, J. K., Soga, K., 2005. *Fundamentals of soil behavior*. John Wiley & Sons, Inc.
- 636 Nguyen, X.P., 2013. Étude du comportement chimico-hydro-mécanique des argiles raides dans
637 le contexte du stockage géologique de déchets radioactifs. Ecole des Ponts ParisTech.
- 638 ONDRAF, 2001. Safety Assessment and Feasibility Interim Report 2 (No. SAFIR2).NIROND
639 2001-06.
- 640 Romero, M.E., 1999. Characterisation and thermo-hydro-mechanical behaviour of unsaturated
641 Boom clay: an experimental study. Universitat Politècnica de Catalunya.
- 642 Skempton, A.W., 1944. Notes on the Compressibility of Clays.”. *Q. J. Geol. Soc. London*, 100(1-
643 4), 119-135.
- 644 Skempton, A.W., 1970. The consolidation of clays by gravitational compaction. *Q. J. Geol. Soc.*,
645 125, 373-411.
- 646 Sridharan, A., Rao, A.S., Sivapullaiah, P.V., 1986. Swelling pressure of clay. *Geotechnical*
647 *Testing Journal*, 9(1), 24-31.
- 648 Sultan, N., Cui, Y.J., Delage, P., 2010. Yielding and plastic behaviour of Boom Clay.
649 *Géotechnique*, 60(9), 657-666.
- 650 Terzaghi, K., Peck, R.B., 1967. *Soil Mechanics in Engineering Practice*. John Wiley London.
- 651 Tran, N.L., 1980. L’essai au bleu de méthylène Un progrès dans la mesure et le contrôle de la
652 propreté des granulats. *Bulletin de liaison des laboratoires des ponts et chaussées*, 107,
653 130-135.

- 654 UCLouvain, 1998. *Rapport d'essai forage Doel-1A*. Laboratoire du Génie Civil, Université
655 Catholique de Louvain.
- 656 Van Marcke, P., 2009. Existing information on the Ypresian clays. In *Meeting on the THMC*
657 *characterisation of Ypresian clays*.
- 658 Van Marcke, P., Laenen, B., 2005. The Ypresian clay as possible host rock for radioactive waste
659 disposal: An evaluation. ONDRAF.
- 660 Vandenberghe, N., 2011. Qualitative & quantitative mineralogical analyses of Ypresian clay.
661 KULeuven.
- 662 Wang, Q., Tang, A.M., Cui, Y.J., Delage, P., Gattmiri, B., 2012. Experimental study on the
663 swelling behaviour of bentonite/claystone mixture. *Engineering Geology*, 124(1), 59-66.
- 664 Wroth, C.P., Wood, D.M., 1978. The correlation of Index Properties with Some Basic
665 Engineering Properties of Soils. *Canadian Geotechnical Journal*, 15, 137-145.
- 666
- 667

668 **7. List of tables**

669 Table 1: Mineralogical composition of Ypresian clays in bulk mass (after Vandenberghe, 2011)

670 Table 2: Mineralogical composition of Ypresian clays in clay-size fraction (after Vandenberghe,
671 2011)

672 Table 3: Physical properties of Ypresian clays

673 Table 4: Test program

674 **8. List of figures**

675 Figure 1: Thickness and depth of the top of Kortrijk formation (After ONDRAF, 2001)

676 Figure 2: Stratigraphical profile and system track of Ypresian clays at Kallo and soil core
677 positions, modified from Cammaer et al. (2009) and Van Marcke & Laenen (2005)

678 Figure 3: Particle-size distribution curves (after Vandenberghe, 2011)

679 Figure 4: Classification of Ypresian clays at Doel and Kallo

680 Figure 5: SEM photos of Ypresian clays at Kallo

681 Figure 6: Pore-size distribution curves of Ypresian clays

682 Figure 7: Vertical stress and displacement variations in high-pressure oedometer test

683 Figure 8: Vertical stress and displacement variations in low-pressure oedometer test

684 Figure 9: Low- (a) and high- (b) pressure oedometer compression curves on YK43

685 Figure 10: Low- (a) and high- (b) pressure oedometer compression curves on YK64

686 Figure 11: Low- (a) and high- (b) pressure oedometer compression curves on YK73

687 Figure 12: Low- (a) and high- (b) pressure oedometer compression curves on YK95

688 Figure 13: Parameter definitions

689 Figure 14: Swelling stress σ_s versus (initial) void ratio (e_i) e for Ypresian clay

690 Figure 15: Variations of C_{se} , C_{ce} (a), C_{sp} and C_{cp} (b) versus preconsolidation stress σ'_p

691 Figure 16: Compression index C_c (a) and yield stress σ'_y (b) profiles

692 Figure 17: Secondary compression/swelling coefficient

693 Figure 18: Permeability of Ypresian clays

694 Figure 19: Hydraulic conductivity profile for Ypresian clays at Doel (after Aertsons et al., 2005)

695 Figure 20: Normalized compression curves

696 Figure 21: Pore-size distribution curves of intact and after HPO test YK73

697 Figure 22: SEM on intact (left) and after LPO test (right) YK43

698

699

700

Table 1: Mineralogical composition of Ypresian clays in bulk mass (after Vandenberghe, 2011)

Core	Depth (m)	Non-clay minerals (wt %)					Clay minerals (wt %)					
		Qtz	Feld.	Car.	Others	Σ_{NC}	Kaol.	Chl.	Sm. Eq.	Ill. Eq.	Σ_C	
YK44	331.48	32	12	2	0.4	46	2	3	33.7	15.3	54	
YK63	350.41	36	13	1.7	1.7	52	5	3	30.8	9.2	48	
YK74	361.29	31	11	0.8	0.4	43	3	4	28.8	21.2	57	
YK96	383.01	27	10	4	0.8	42	3	3	30.4	22.6	59	

701

702

Table 2: Mineralogical composition of Ypresian clays in clay-size fraction (after Vandenberghe, 2011)

Core	Relative to clay-size fraction (wt %)								Relative to total mass (wt %)				
	Ill.-Sm. (wt %) (%Sm.)		Ill.	Sm.	Kaol.	Chl.	$\Sigma Sm.$	$\Sigma 2:1$	$\Sigma 2:1$	Ill.-Sm.	Ill.	Sm.	$\Sigma Sm.$
YK44	24	38	9	63	2	2	72	96	49	12	5	32	37
YK63	24	33	9	62	1	4	70	95	40	10	4	26	29
YK74	22	38	10	63	2	3	71	95	50	12	5	33	38
YK96	23	37	10	59	3	5	68	92	53	13	6	34	39

703

704

705

706

707

Qtz: Quartz; Feld.: Feldspar; Car.: Carbonates; Others: Plagioclase, dolomite, Pyrite, Anatase, Opal CT and Zeolite; Σ_{NC} : Total non-clay minerals; Kaol.: Kaolinite; Chl.: Chlorite; Sm. Eq. = equivalent of smectite in the bulk rock based on the CEC results assuming an average smectite with a charge of 100meq/100g; Ill. Eq. = equivalent of illite/muscovite in the bulk rock calculated as $\Sigma 2:1$ - sm. Eq; $\Sigma 2:1$: di-octahedral clays (illite, smectite, illite-smectite, glauconite) and micas; ΣC : Total clay minerals; $\Sigma Sm.$ = Sm. + Ill.-Sm. \times %Sm., is the total smectite content

708

709

710

711

712

713

714

715

716

Table 3: Physical properties of Ypresian clays

Core	YK43	YK64	YK73	YK95
G_s (-)	2.776	2.785	2.802	2.802
ρ_0 (Mg/m ³)	1.97 ± 0.03	1.97 ± 0.01	1.9 ± 0.01	1.91 ± 0.05
ρ_{d0} (Mg/m ³)	1.57	1.55	1.43	1.47
e_0 (-)	0.77 ± 0.03	0.79 ± 0.03	0.95 ± 0.06	0.90 ± 0.06
n_0 (%)	44 ± 1.1	44 ± 1.1	49 ± 1.6	47 ± 1.5
LL (-)	75.07	113.84	136.61	132.22
PL (-)	33.50	33.75	36.08	43.75
PI (-)	41.57	80.09	100.53	88.47
w_0 (%)	25.78 ± 0.73	26.74 ± 1.86	32.01 ± 1.56	29.78 ± 1.94
S_{r0} (%)	93 ± 3	95 ± 4	96 ± 4	93 ± 5
S_s (m ² /g)	83	149	275	267
VBS (g/100 g)	3.95	7.09	13.12	12.72
% CaCO ₃ (g/100 g)	10.2	1.4	0.9	3.8

717

718

719

Table 4: Test program

Core	Test	w_0 (%)	e_0 (-)	n_0 (%)	S_{r0} (%)	ρ_0 (Mg/m ³)	$e_{\sigma'v0}$ (-)
43	YK43O1	26.04	0.81	45	89	1.94	0.70
	YK43O2	25.05	0.78	44	89	1.95	0.64
64	YK64O1	26.22	0.79	44	92	1.96	0.74
	YK64O2	27.65	0.80	44	97	1.98	0.73
73	YK73O1	31.09	0.94	48	93	1.89	0.82
	YK73O2	31.36	0.93	48	95	1.91	0.80
95	YK95O1	29.72	0.95	49	87	1.86	0.80
	YK95O2	31.73	0.94	49	94	1.90	0.80

720

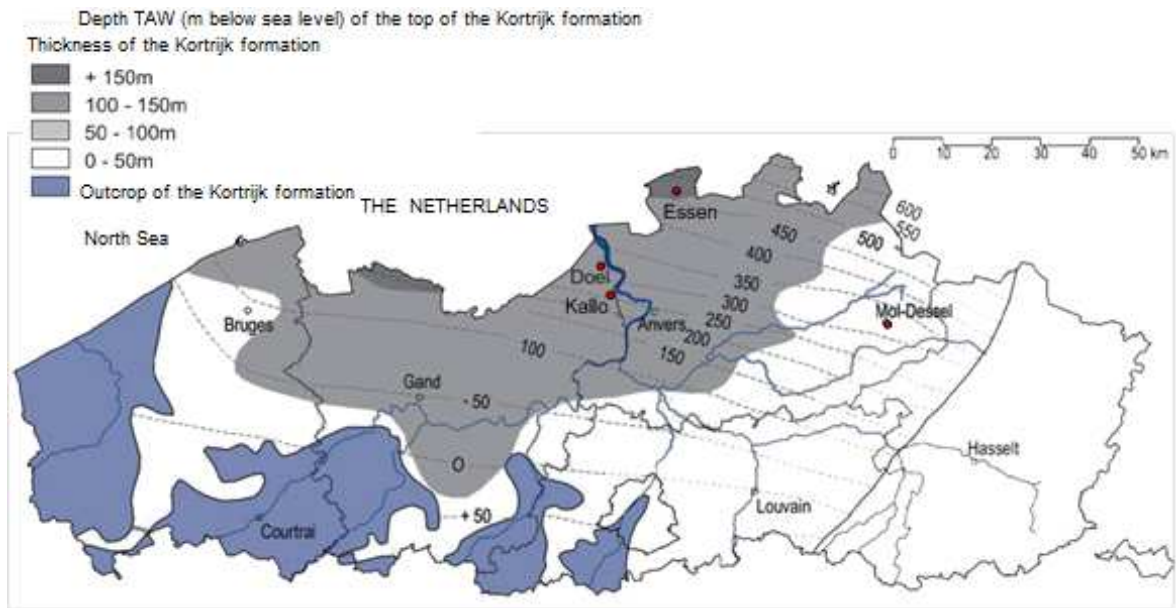


Figure 1: Thickness and depth of the top of Kortrijk formation (After ONDRAF, 2001)

721

722

723

724

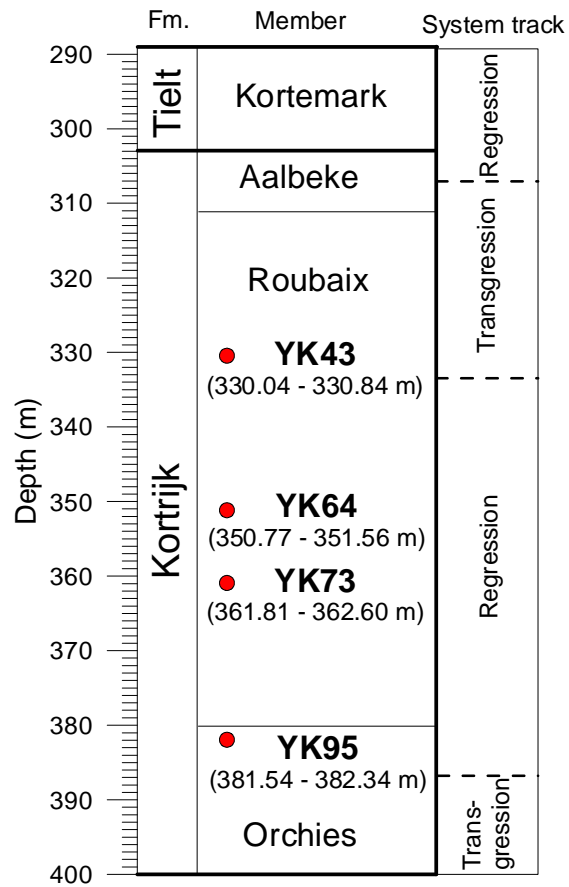


Figure 2: Stratigraphical profile and system track of Ypresian clays at Kallo and soil core positions, modified from Cammaer et al. (2009) and Van Marcke & Laenen (2005)

725
726
727
728

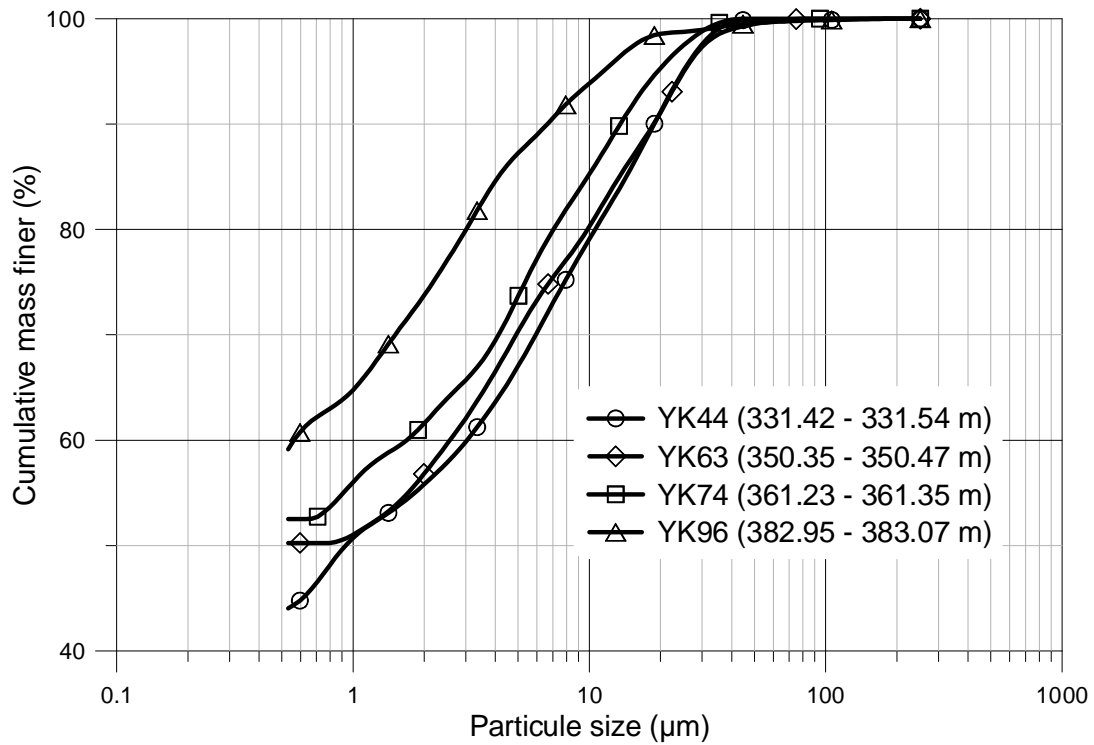


Figure 3: Particle-size distribution curves (after Vandenberghe, 2011)

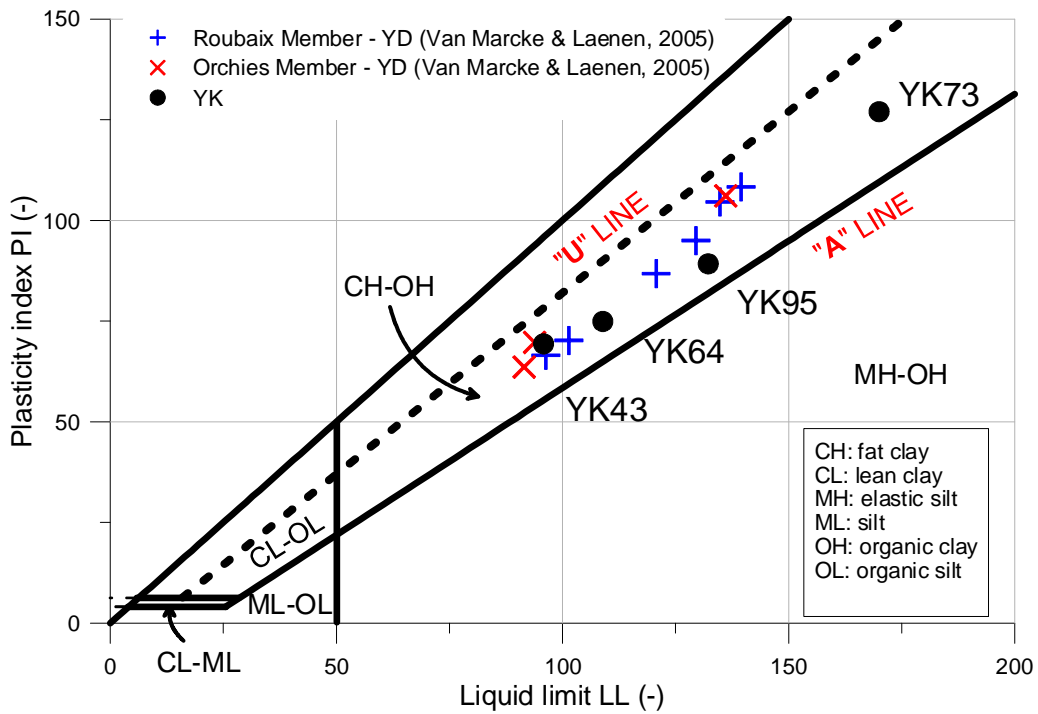
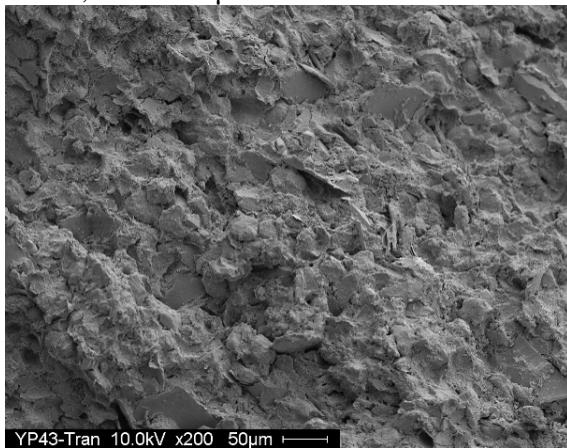


Figure 4: Classification of Ypresian clays at Doel and Kallo

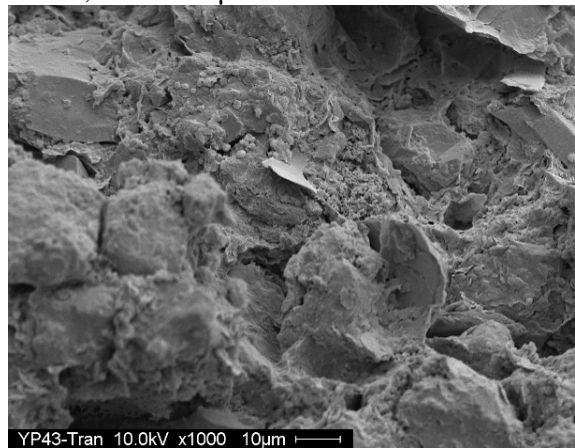
729
730
731

732
733

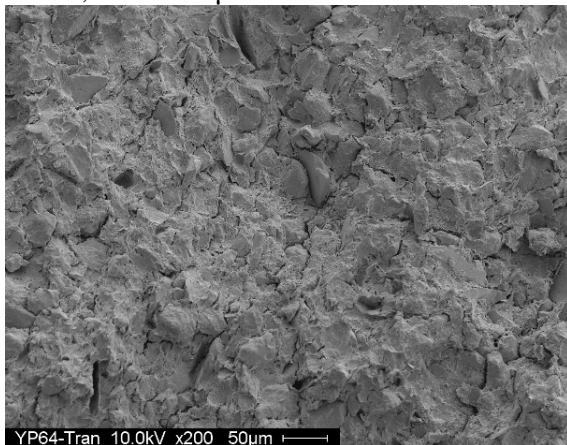
YK43, 625×500 μm



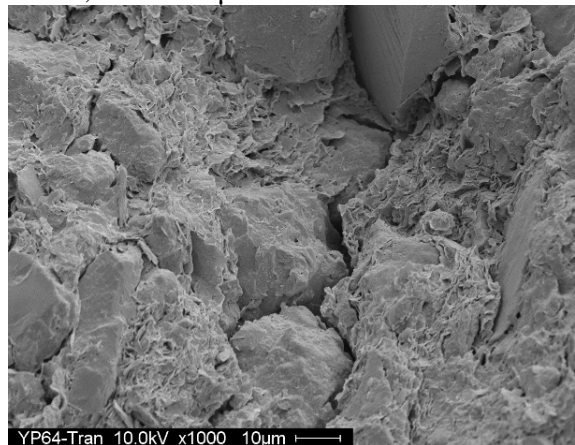
YK43, 125×100 μm



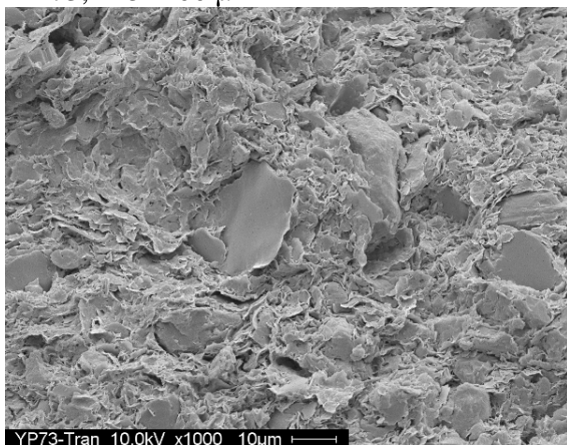
YK64, 625×500 μm



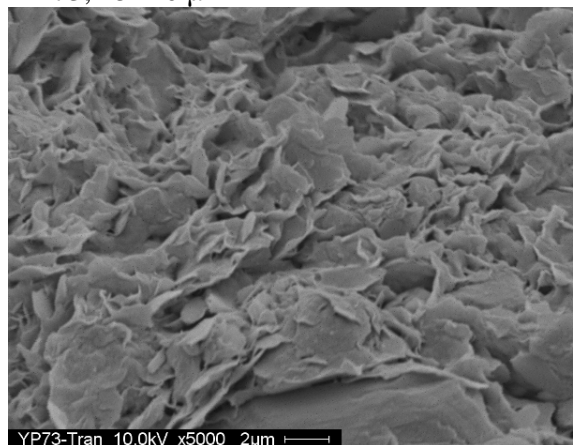
YK64, 125×100 μm



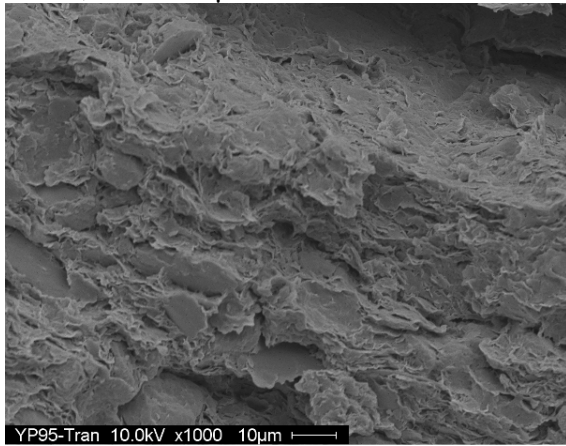
YK73, 125×100 μm



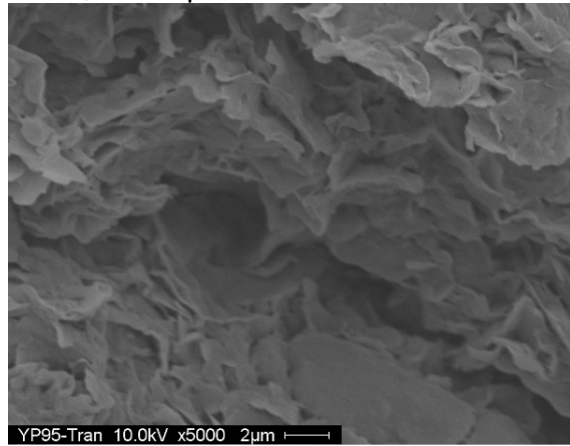
YK73, 25×20 μm



YK95, 125×100 μm



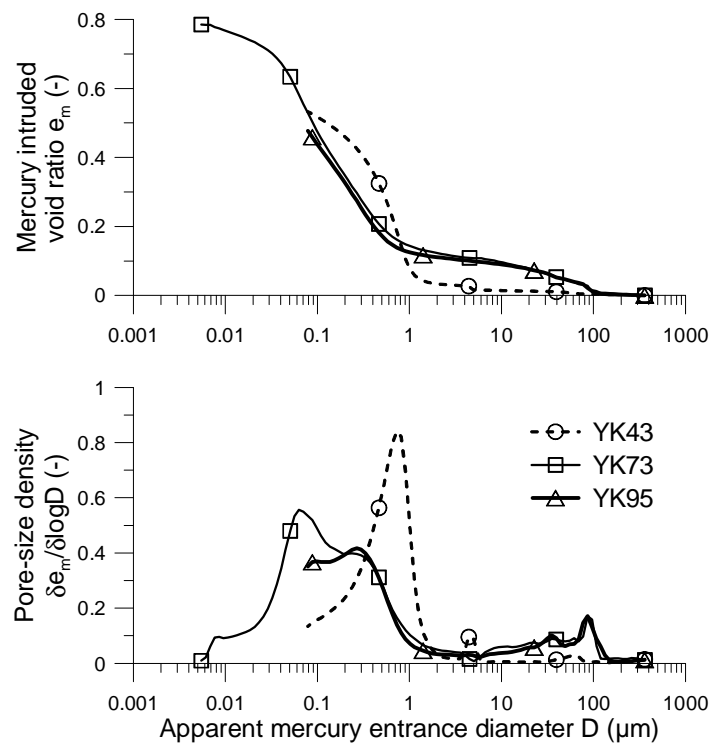
YK95, 25×20 μm



734

Figure 5: SEM photos of Ypresian clays at Kallo

735

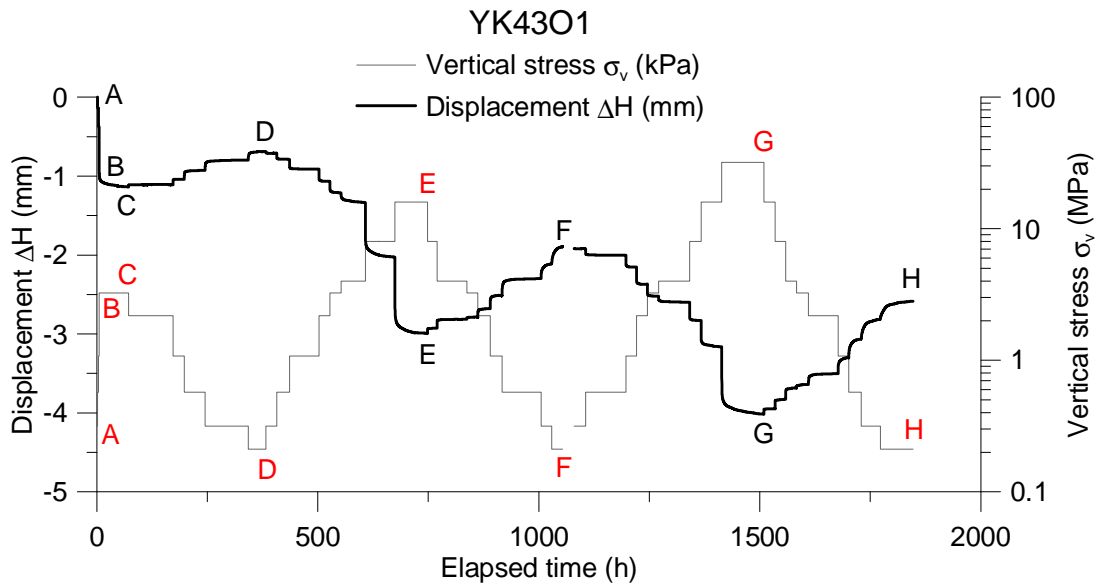


736

737

Figure 6: Pore-size distribution curves of Ypresian clays

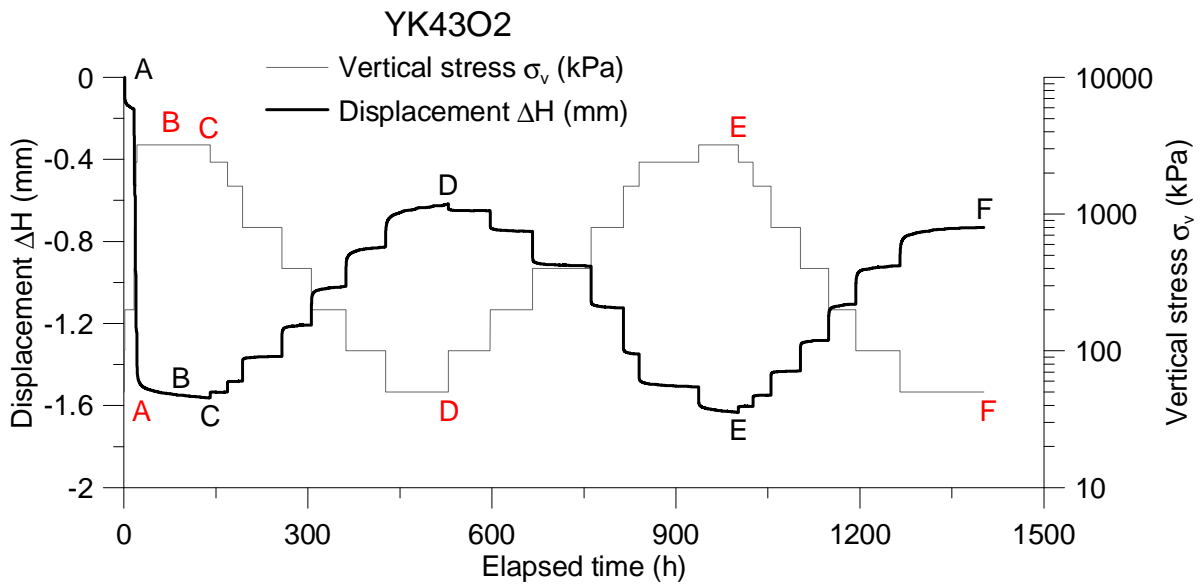
738



739
740

Figure 7: Vertical stress and displacement variations in high-pressure oedometer test

741



742
743

Figure 8: Vertical stress and displacement variations in low-pressure oedometer test

744

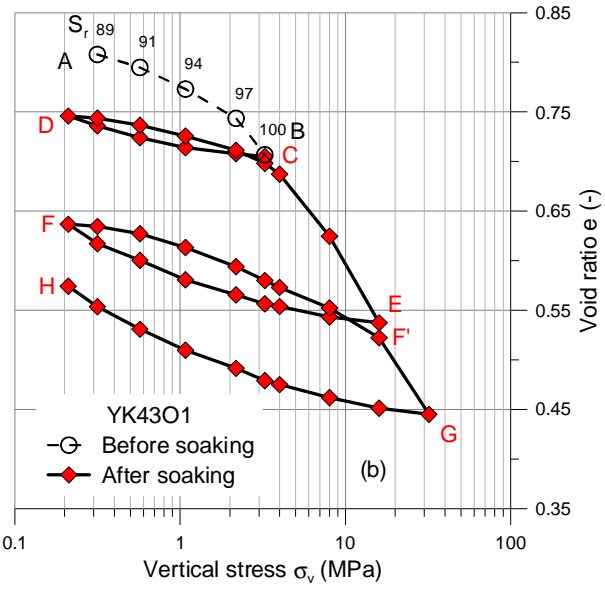
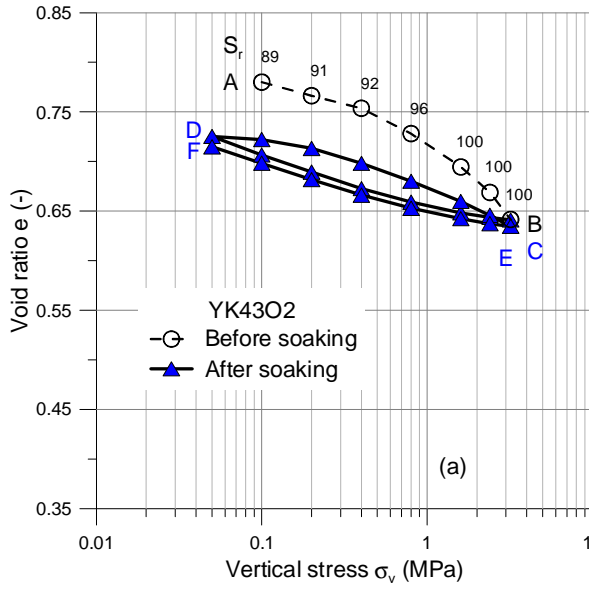


Figure 9: Low- (a) and high- (b) pressure oedometer compression curves on YK43

745
746

747

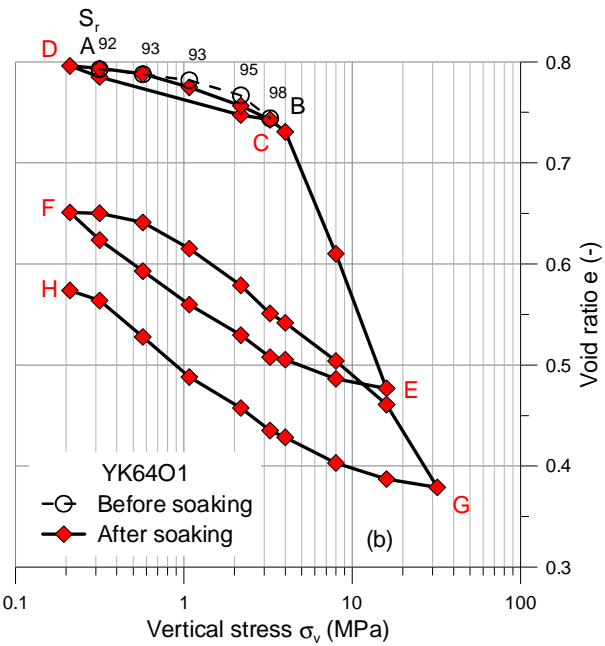
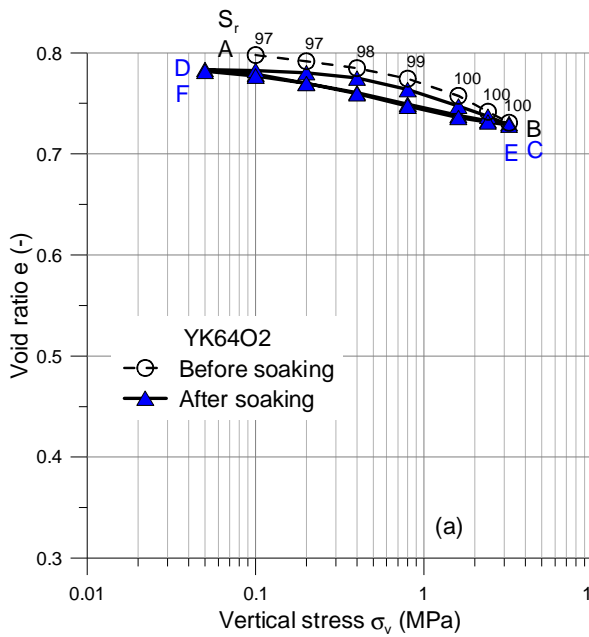


Figure 10: Low- (a) and high- (b) pressure oedometer compression curves on YK64

748
749

750

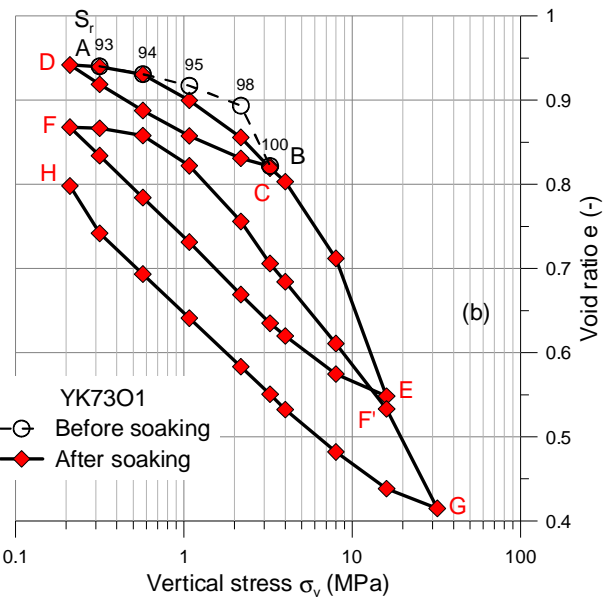
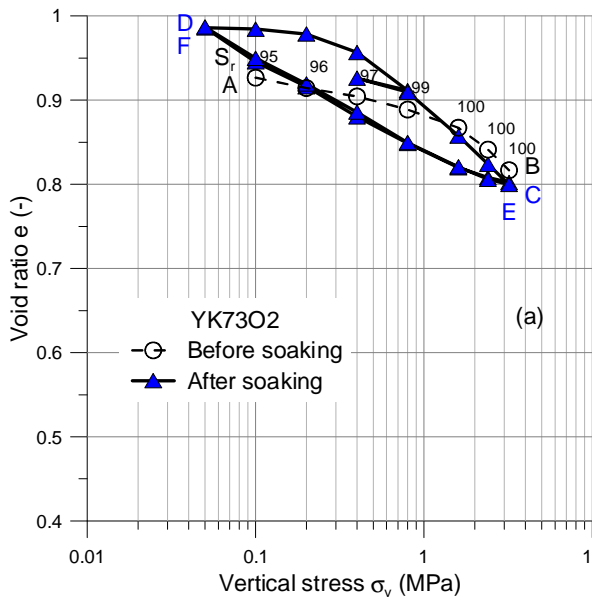


Figure 11: Low- (a) and high- (b) pressure oedometer compression curves on YK73

751
752

753

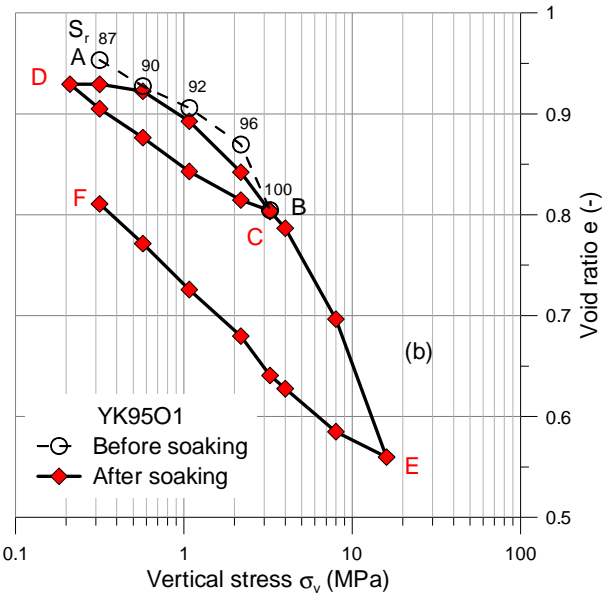
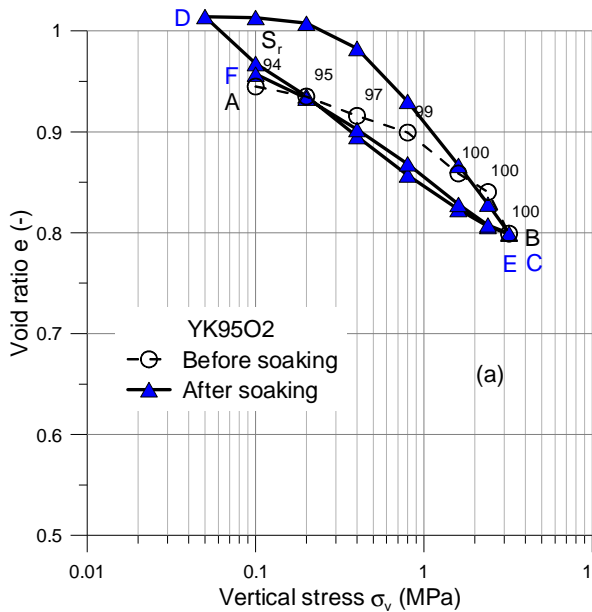


Figure 12: Low- (a) and high- (b) pressure oedometer compression curves on YK95

754
755

756

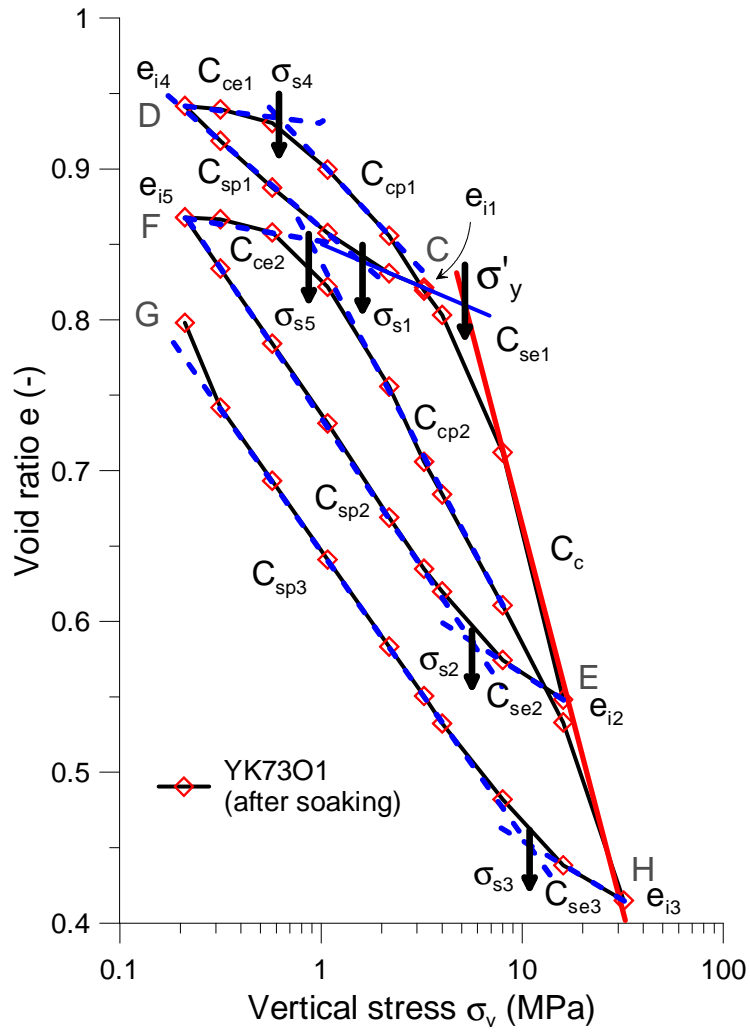


Figure 13: Parameter definitions

757
758
759

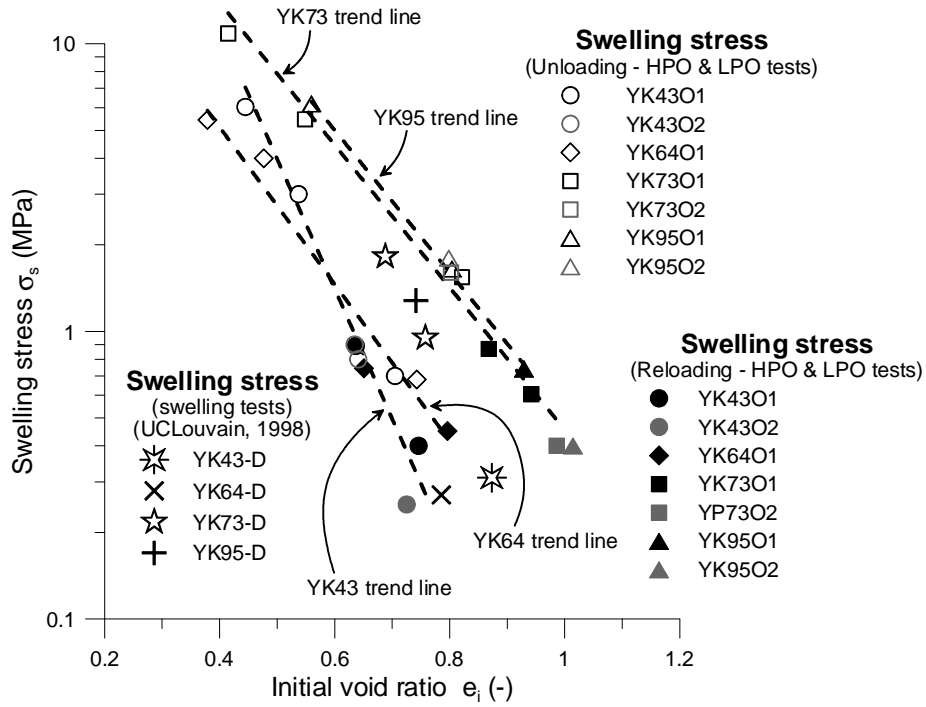


Figure 14: Swelling stress σ_s versus (initial) void ratio (e_i) e for Ypresian clay

760
761
762

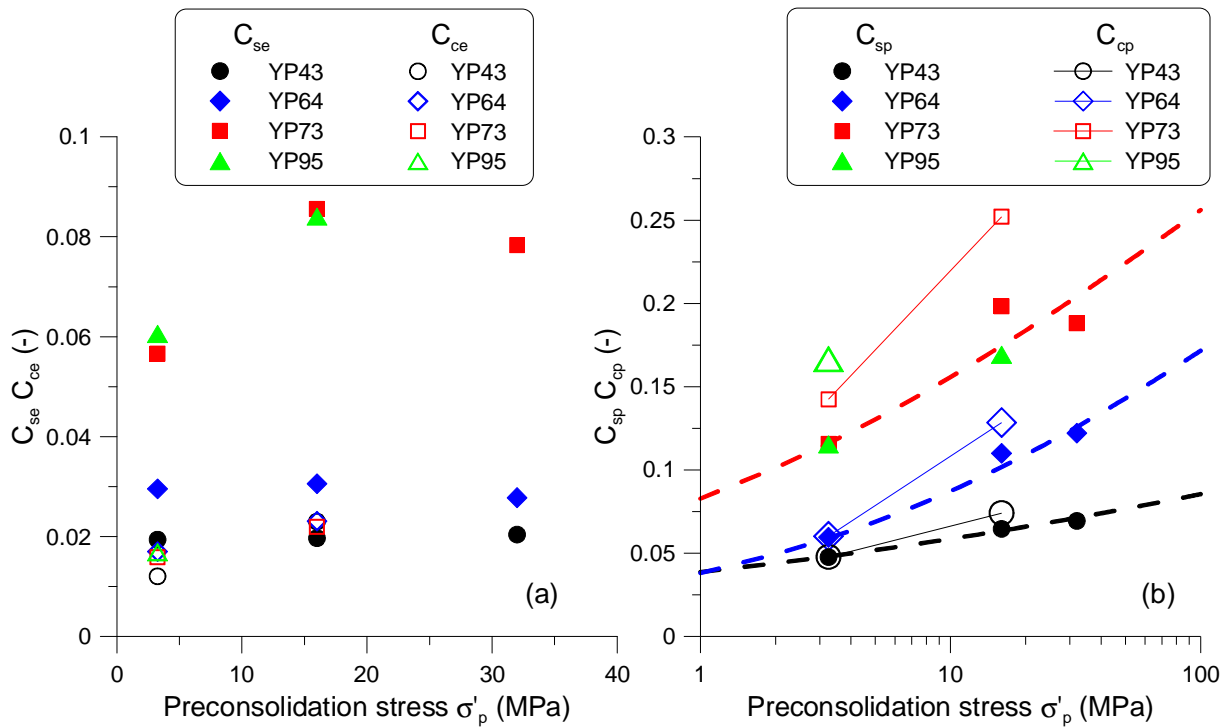


Figure 15: Variations of C_{se} , C_{ce} (a), C_{sp} and C_{cp} (b) versus preconsolidation stress σ'_p

763
764
765

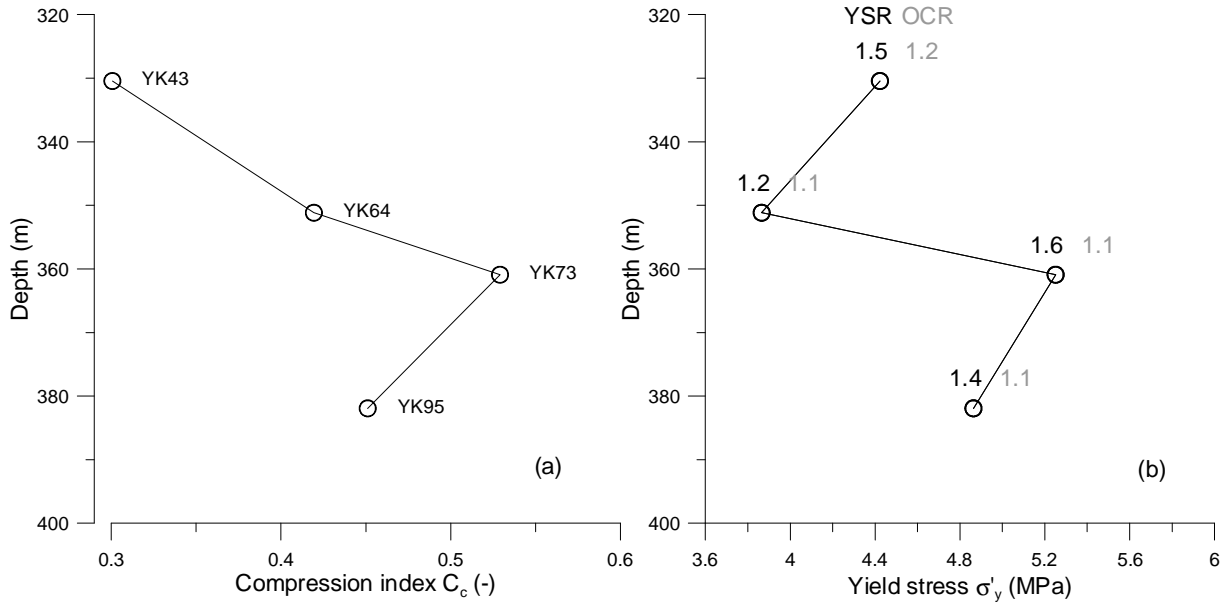


Figure 16: Compression index C_c (a) and yield stress σ'_y (b) profiles

766
767
768

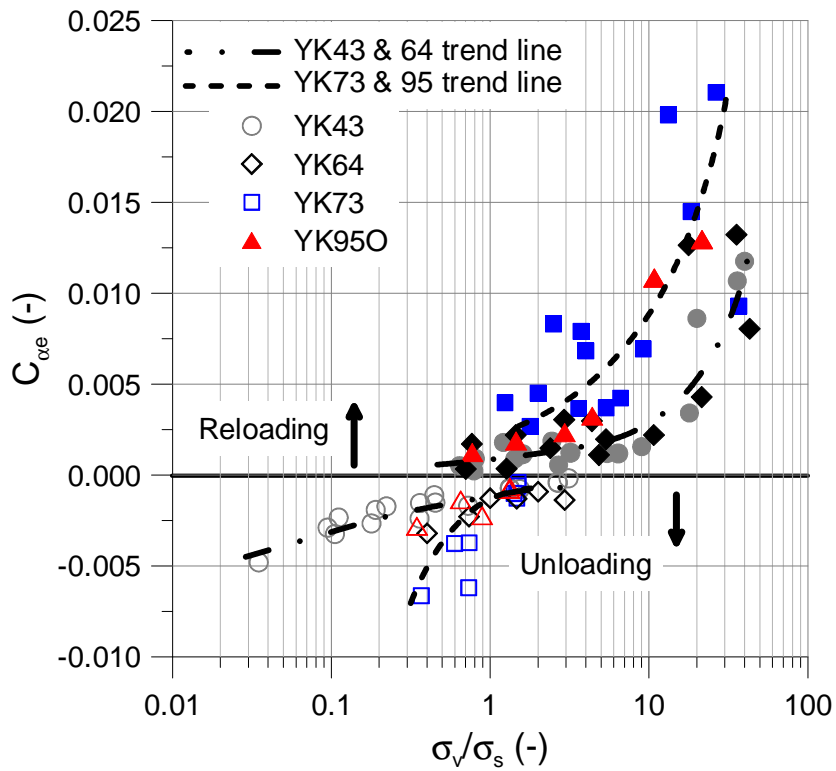


Figure 17: Secondary compression/swelling coefficient

769
770
771

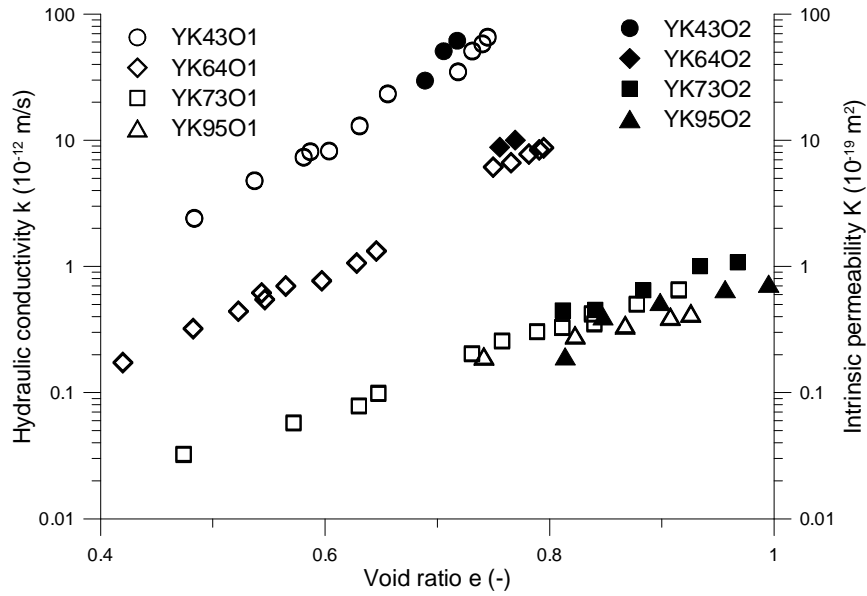


Figure 18: Permeability of Ypresian clays

772
773
774

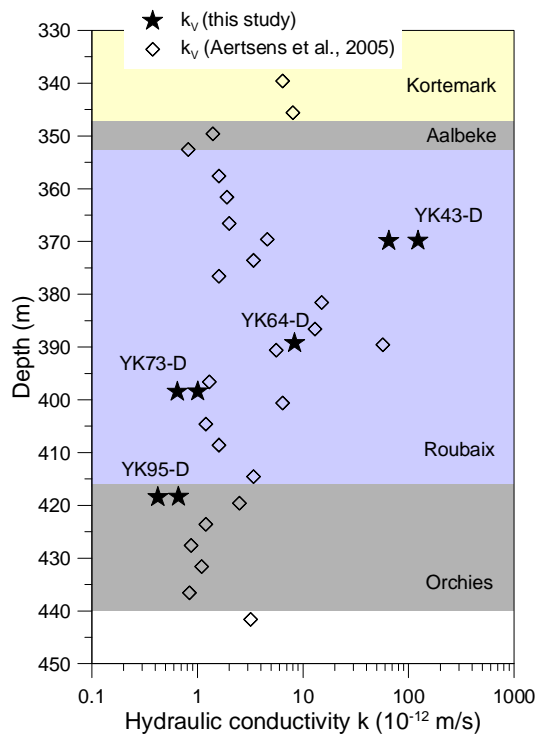


Figure 19: Hydraulic conductivity profile for Ypresian clays at Doel (after Aertsons et al., 2005)

775
776
777

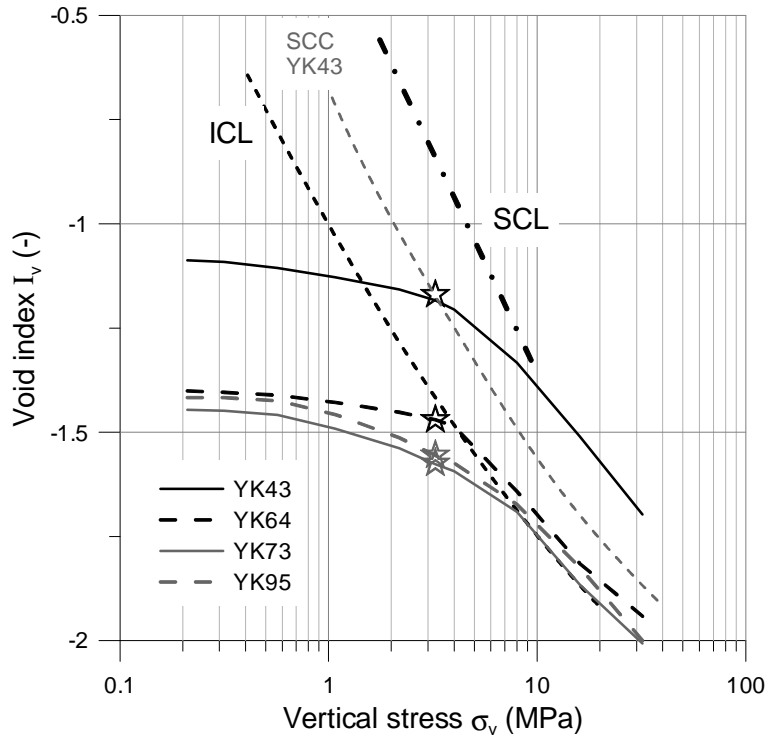


Figure 20: Normalized compression curves

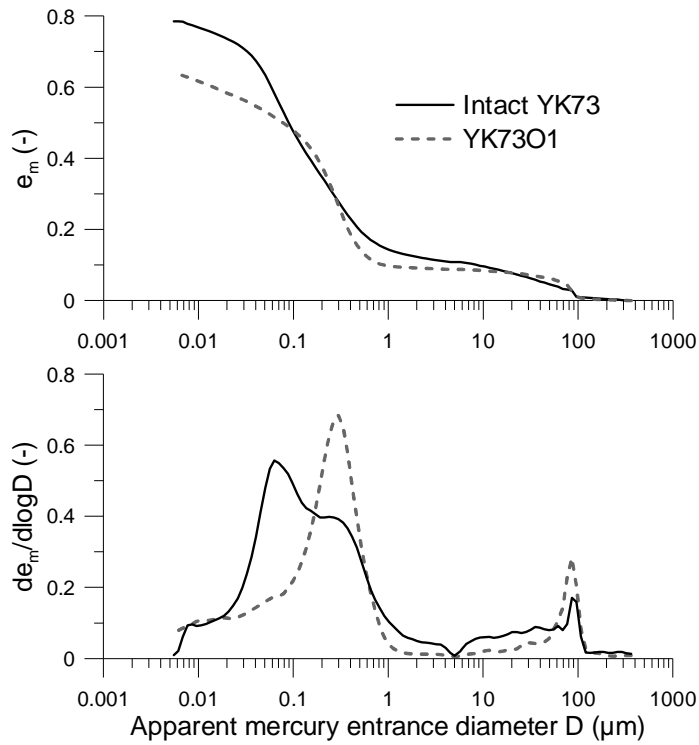


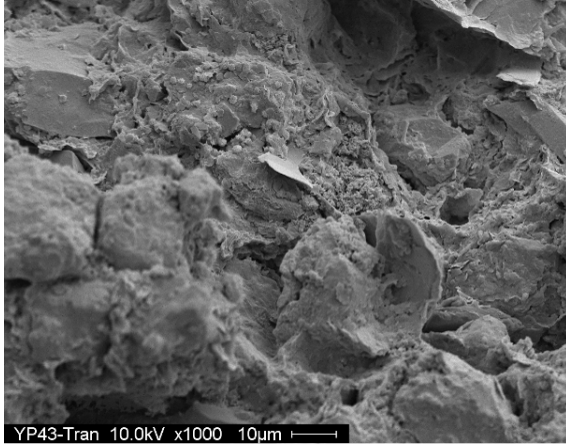
Figure 21: Pore-size distribution curves of intact and after HPO test YK73

778
779

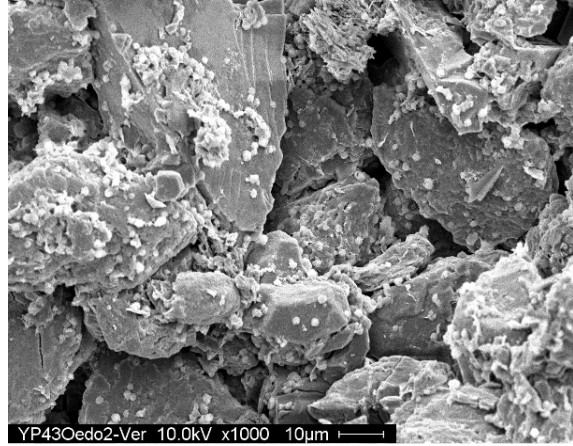
780

781
782

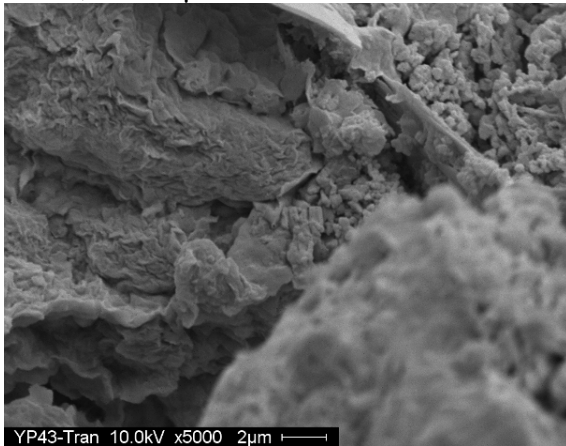
YK43, 125×100 μm



YK43O2, 125×100 μm



YK43, 25×20 μm



YK43O2, 25×20 μm

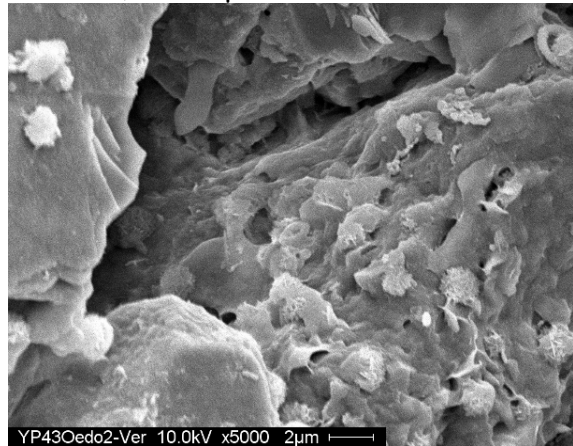


Figure 22: SEM on intact (left) and after LPO test (right) YK43